

Tuning of Cr–Cr Magnetic Exchange through Chalcogenide Linkers in Cr₂ Molecular Dimers

Eranga H. Gamage, Raquel A. Ribeiro, Colin P. Harmer, Paul C. Canfield, Andrew Ozarowski,* and Kirill Kovnir*



Cite This: *Inorg. Chem.* 2022, 61, 6160–6174



Read Online

ACCESS |



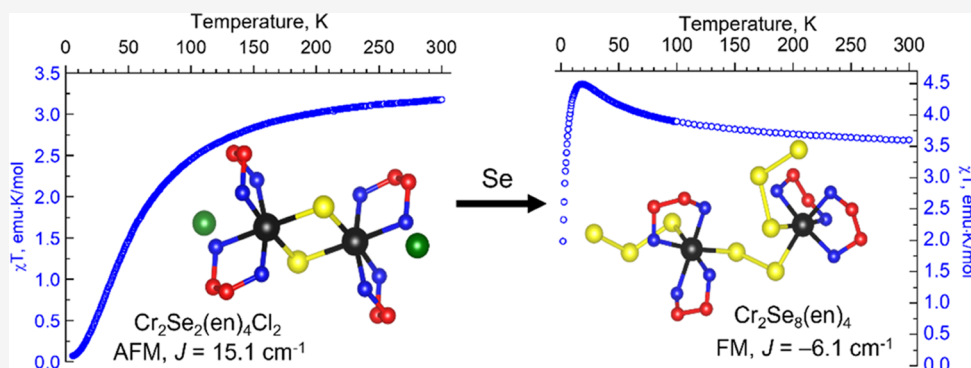
Metrics & More



Article Recommendations



Supporting Information



ABSTRACT: A set of three Cr-dimer compounds, Cr₂Q₂(en)₄X₂ (Q: S, Se; X: Br, Cl; en: ethylenediamine), with monoatomic chalcogenide bridges have been synthesized via a single-step solvothermal route. Chalcogenide linkers mediate magnetic exchange between Cr³⁺ centers, while bidentate ethylenediamine ligands complete the distorted octahedral coordination of Cr centers. Unlike the compounds previously reported, none of the chalcogenide atoms are connected to extra ligands. Magnetic susceptibility studies indicate antiferromagnetic coupling between Cr³⁺ centers, which are moderate in Cr₂Se₂(en)₄X₂ and stronger in Cr₂S₂(en)₄Cl₂. Fitting the magnetic data requires a biquadratic exchange term. High-frequency EPR spectra showing characteristic signals due to coupled *S* = 1 spin states could be interpreted in terms of the “giant spin” Hamiltonian. A fourth compound, Cr₂Se₈(en)₄, has a single diatomic Se bridge connecting the two Cr³⁺ centers and shows weak ferromagnetic exchange interactions. This work demonstrates the tunability in strength and type of exchange interactions between metal centers by manipulating the interatomic distances and number of bridging chalcogenide linkers.

INTRODUCTION

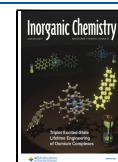
Since the successful studies of copper acetate monohydrate by electronic paramagnetic resonance (EPR),^{1,2} accompanied by important theoretical work,³ extensive research has been performed on a wide variety of binuclear or polynuclear complexes with various mono- or polyatomic bridges.^{4–8} A theoretical analysis demonstrated that the bridging species significantly influence the Jahn–Teller distortion associated with the metal centers.⁹ A computational study based on extended Hückel type calculations conducted by Hoffman et al. showed that the metal–metal interactions in bridged dimer complexes are facilitated by coupling through the orbitals of the bridging groups.¹⁰ As a result of these findings, scientists gained insight into the role of many biologically important d-block metal dimeric compounds with respect to metabolism, catalysis, and drug delivery. Many oxo-bridged transition-metal dimers have been theoretically studied as molecular magnetic materials to elucidate their nearest neighbor interactions.¹¹ Ruthenium dimers are extensively studied for their ability to catalyze water oxidation^{12,13} and as promising pharmaceutical

candidates.^{14,15} Binuclear cobalt complexes have been shown as promising agents for electrocatalytic proton reduction¹⁶ and slow magnetic relaxation.^{17,18} Gennari and Duboc et al. discovered a non-Heme manganese dimer capable of effectively reacting with oxygen,¹⁹ while exchange and magnetic anisotropy effects were studied in several different manganese dimers.^{20,21} A vast majority of dimer-related research is focused on copper dimers for their susceptibility to being bridged by diverse bulky organic ligands resulting in a variety of magnetic and superexchange interactions.^{22–26}

Complexes where transition-metal atoms are bridged by heavier elements with stronger spin–orbit coupling are

Received: January 27, 2022

Published: April 12, 2022



relatively rare and have not been intensively investigated. Lledos et al. reported an *ab initio* study on Pt₂S₂ rings to understand the factors that govern the structural preferences.²⁷ Magnetic susceptibility and Mössbauer experiments demonstrated the presence of mixed-valent [Fe₂S₂]⁺ dimers in iron–sulfur clusters in ferredoxins and other biological systems.^{28–30} Binuclear complexes of many-electron metals like Cr are much more challenging to characterize, particularly from the viewpoint of EPR as a large zero-field splitting is often observed, making the standard X- or even Q-Band EPR inaccessible.^{31–33} Despite this, extensive magnetic and EPR studies have been conducted on different kinds of Cr^{III}–Cr^{III} dimers bridged by a variety of organic moieties following both experimental^{34–39} and theoretical approaches.^{40–44} Semenaka et al. investigated the Cr–Cr interactions in the weakly exchange-coupled alkoxo-bridged heterometallic Zn₂Cr₂ complexes by means of magnetometry, high-frequency EPR spectroscopy, and density functional theory (DFT) calculations.⁴⁵

The possibility of utilizing selenium bridged transition-metal dimer complexes as catalysts for organic reactions has been studied over the past few decades.^{46–50} Chemistry of the linear Cr₂Se and butterfly Cr₂Se₂ complexes has been explored by different synthetic and characterization approaches.^{51–53} In this work, we report the synthesis, crystal structure, and properties of three new molecular compounds Cr₂Q₂(en)₄X₂ (Q: S, Se; X: Br, Cl; en: ethylenediamine), all with a Cr₂Q₂ rhombus core. An important feature of these compounds is that the bridging selenium atoms are not connected to any other organic ligands. Magnetic studies coupled with high-frequency EPR reveal antiferromagnetic interactions between Cr centers in Cr₂Q₂(en)₄X₂. A reaction of Cr₂Se₂(en)₄Br₂ with excess Se resulted in the formation of another Cr₂ compound with a diatomic selenium bridge, Cr₂Se₈(en)₄, previously reported by Dehnen et al.⁵⁴ Magnetic susceptibility studies show that the replacement of the monoatomic Se bridge with the diatomic one leads to the change of the type of Cr–Cr interactions from antiferromagnetic to ferromagnetic.

EXPERIMENTAL SECTION

Warning: Reactions conducted with Se using amine solvents can give out toxic fumes. Opening of the reaction autoclaves should only be done in well-ventilated areas, like a fumehood. Splashing of the solvent may occur upon opening the autoclaves. Wearing proper protective equipment including face-shields, long-sleeve gloves, and tight-cuff lab coats and placing the furnaces in well-ventilated spaces such as fume hoods is highly recommended. Filtration of the samples and further sample handling should be conducted in a fumehood with emergency exhaust activated due to the strong odor.

Synthesis of Cr₂Se₂(en)₄X₂ (X = Br, Cl). Cr₂Se₂(en)₄Br₂ was synthesized by the reaction of 1 mmol of chromium powder (–100 + 325 mesh, Alfa Aesar, 99.97%) and 1 mmol of selenium powder (Sigma-Aldrich, >99.5%) with 100 mg of ammonium bromide (Alfa Aesar, 99%) in 10 mL of ethylenediamine (en) (Alfa Aesar, 99%) under solvothermal conditions for 3–5 days at 200 °C. After which, the autoclave vessel was cooled naturally to room temperature in the fumehood. The product was then filtered with aliquots of absolute ethanol and appeared as black shiny needles with silver chunks (Figure S1). The silvery chunks were identified to be recrystallized chromium as indicated by the peak at 2θ = 44.4° attributed to elemental chromium in the powder X-ray diffraction (PXRD) pattern. The Cr₂Se₂(en)₄Br₂ crystals looked dull green in color when finely ground. The chloride analogue Cr₂Se₂(en)₄Cl₂ was formed under similar conditions when ammonium bromide was replaced with ammonium chloride (Fisher Scientific, 99%).

Cr₂Se₂(en)₄Br₂ and Cr₂Se₂(en)₄Cl₂ were also synthesized when the Cr metal was replaced with chromium (III) bromide hexahydrate (Strem Chemicals, Incorporated, 99%) and chromium (III) chloride hexahydrate (Alfa Aesar, 98%), respectively, in the presence of respective NH₄X (Table S1). Using hydrous Cr halides, experiments were conducted to optimize the reaction conditions that would result in no residual elemental Cr in the final product. During the optimization process, the samples were visually examined under the optical microscope to check for recrystallized chunks of elemental Cr and the appearance of the Cr peak in the PXRD pattern was monitored. The final optimized reaction conditions: solvothermal reaction of 1 mmol hydrous Cr halide, 1.33 mmol Se, and 150 mg of the corresponding NH₄X in 10 mL of en for 3–5 days at 200 °C. Such reactions provided samples with no detected Cr impurity and were used for property measurements. All of the reactions were carried out under normal atmospheric conditions and the resulting samples could be stored in vials on the benchtop for several months with no signs of decomposition or oxidation.

Synthesis of Cr₂S₂(en)₄Cl₂. The sulfur analogue, Cr₂S₂(en)₄Cl₂, was synthesized by a reaction of chromium (III) chloride hexahydrate and sulfur powder (–100 mesh, Alfa Aesar, 99.5%) in a 1:1 molar ratio with 100 mg of ammonium chloride added to en solution (Table S1). Reactions were prepared and processed under the conditions mentioned above, yielding a dark shiny green-black powder that gave an experimental PXRD pattern resembling its calculated pattern. For the synthesis of Cr₂S₂(en)₄Cl₂, thiourea (Sigma-Aldrich, 99%) can also be used as the source of sulfur in a 1:2 molar ratio. In turn, reactions of metallic chromium powder with sulfur powder failed to yield the dimer phase and resulted in recrystallized chromium as the only solid product. Due to the inability to grow single crystals of Cr₂S₂(en)₄Cl₂, the crystal structure was established by high-resolution synchrotron powder X-ray diffraction. All attempts to synthesize the bromide analogue of Cr₂S₂(en)₄Cl₂ were unsuccessful.

Synthesis of Cr₂Se₈(en)₄. Treatment of the Cr₂Se₂(en)₄Br₂ phase with selenium (1:8 molar ratio) in an excess of en under similar solvothermal conditions at 200 °C led to the formation of the Cr₂Se₈(en)₄ phase (Table S1). The reaction vessel was cooled naturally to room temperature and the products were filtered with absolute ethanol. Cr₂Se₈(en)₄ crystallizes as shiny black crystals (~1 mm³) forming clusters clearly visible to the naked eye (Figure S2). The sample was dried on a Petri dish under normal atmospheric conditions after which the crystals were handpicked and finely ground for property measurements.

Characterization. All Cr₂Q₂(en)₄X₂ (Q = S, Se; X = Br, Cl) and Cr₂Se₈(en)₄ samples were synthesized outside the glovebox due to their air and moisture stability. After filtration, the samples were stored in vials and kept on a benchtop under ambient conditions. PXRD experiments were conducted on a benchtop Rigaku 600 Miniflex with a Cu K_α radiation (λ = 1.54185 Å) and a Ni K_β filter. Fluorescence of Cr atoms in the sample upon exposure to incident Cu K_α radiation, grease used to stick powder to the plate, or the presence of trace amorphous impurities contribute to the background in the PXRD patterns.

In-situ PXRD experiments were conducted on beamline 17-BM-B (λ = 0.24153 Å) at the Advanced Photon Source (APS) in the Argonne National Laboratory (ANL) using the solvothermal setup we reported earlier.⁵⁵ High-resolution synchrotron PXRD data was obtained through the mail-in program on beamline 11-BM-B (λ = 0.457910 Å) at the APS. A powdered sample of Cr₂S₂(en)₄Cl₂ was packed in a 0.8 mm Kapton capillary to conduct a ~1 h scan in the 0.5° < 2θ < 50° range at 100 K and Rietveld refinement was performed on the data using GSAS-II software to determine the crystal structure.⁵⁶ The initial model derived from the Se analog was used for refinement against the high-resolution synchrotron powder data.

Single-crystal diffraction data were collected on a Bruker D8 Venture diffractometer with a Photon100 CMOS detector employing Mo K_α radiation (λ = 0.71073 Å) at 100 K under a constant flow of dry N₂. Crystal structure refinement was performed using the SHELXL software package.⁵⁷

Magnetic measurements were performed on ~40 mg of powdered samples with a Quantum Design SQUID magnetometer MPMS-5. The temperature dependence of magnetization was studied in different applied magnetic fields. Isothermal field dependence of the magnetization was studied in a 0–7 T field at different temperatures. A nonlinear least-squares method was used to fit the magnetic data as described in the [Magnetic Properties](#) section.

Elemental composition data of the samples were obtained on an Energy Dispersive X-ray Spectrometer FEI Quanta 250 field emission-SEM with EDS detection (Oxford X-Max 80) and Aztec software was used for data analysis. Needles of $\text{Cr}_2\text{Se}_2(\text{en})_4\text{Br}_2$, $\text{Cr}_2\text{Se}_2(\text{en})_4\text{Cl}_2$ and chunks of $\text{Cr}_2\text{Se}_8(\text{en})_4$ were mounted onto graphite tape for analysis. Normalization of quants obtained at different acquisition sites provided the average composition to be $\text{Cr}_{1.9(1)}\text{Se}_2\text{Br}_{1.9(5)}$, $\text{Cr}_{1.9(3)}\text{Se}_2\text{Cl}_{2.0(4)}$, and $\text{Cr}_{1.9(9)}\text{Se}_8$ based on normalization to the Se content obtained from crystal structure models. Quants obtained for $\text{Cr}_2\text{S}_2(\text{en})_4\text{Cl}_2$ powder on carbon tape yielded a normalized composition of $\text{Cr}_{1.9(1)}\text{S}_2\text{Cl}_{2.0(1)}$.

The high-field, high-frequency EPR spectra at temperatures ranging from ca. 3 to 290 K were recorded on a home-built spectrometer at the EMR facility of the National High Magnetic Field Laboratory (NHMFL).⁵⁸ The instrument is equipped with a superconducting magnet (Oxford Instruments) capable of reaching a field of 17 T. Microwave frequencies over the range 52–630 GHz were generated by a phase-locked Virginia Diodes source, producing a base frequency of 8–18 GHz, which was multiplied by a cascade of frequency multipliers. The instrument is a transmission-type device and uses no resonance cavity. The EPR spectra and magnetic data were simulated using software written by AO, available from the author upon request.

RESULTS AND DISCUSSION

Synthesis of $\text{Cr}_2\text{Se}_2(\text{en})_4\text{X}_2$. $\text{Cr}_2\text{Se}_2(\text{en})_4\text{X}_2$ ($X = \text{Cl}, \text{Br}$) compounds were first synthesized using elemental chromium as the precursor, which led to the presence of residual chromium metal in the final products. Notable differences in the intensities of peaks between theoretical and experimental PXRD patterns in $\text{Cr}_2\text{Se}_2(\text{en})_4\text{X}_2$ are a result of the preferred orientation of the needle-like crystals ([Figure S3](#)). To remove the Cr metal admixture, optimization reactions were carried out by varying the reaction conditions such as elemental ratios and concentrations, reaction duration, temperature, filling fraction of the solvent, and cooling rates ([Table S1](#)). But all of these attempts failed to deliver a phase-pure product with no chromium impurity. However, these optimizations did reveal that $\text{Cr}_2\text{Se}_2(\text{en})_4\text{X}_2$ had a formation window of 180 to 230 °C.

Post-synthetic recrystallization of $\text{Cr}_2\text{Se}_2(\text{en})_4\text{Br}_2$ was attempted. The compound was not soluble in methanol, ethanol, ethanolamine, dimethylformamide (DMF), dimethyl sulfoxide (DMSO), and diethyl ether. When ethylenediamine was mixed with aqueous potassium hydroxide/glycerol/ethylene glycol, the resulting solvents decomposed the dimer into constituent elements upon heating and stirring. The universal solvent, water, was able to completely dissolve $\text{Cr}_2\text{Se}_2(\text{en})_4\text{Br}_2$. However, in the case of water, the compound did not precipitate out from the cooled filtrate and instead disintegrated into elemental Cr and Se. Since the recrystallization attempts failed, attention was diverted to using different starting materials. When metallic Cr was replaced by soluble Cr salts under the same conditions, $\text{Cr}_2\text{Se}_2(\text{en})_4\text{Br}_2$ was synthesized as a black powder with minimum chromium impurity as evidenced by the PXRD patterns ([Figure 1](#)). Samples synthesized in this manner turned out to be black powders with no residual elemental chromium.

To gain insight into the mechanism of formation of $\text{Cr}_2\text{Se}_2(\text{en})_4\text{Br}_2$, *in-situ* powder X-ray diffraction studies were conducted at the 17-BM Advanced Photon Source of the

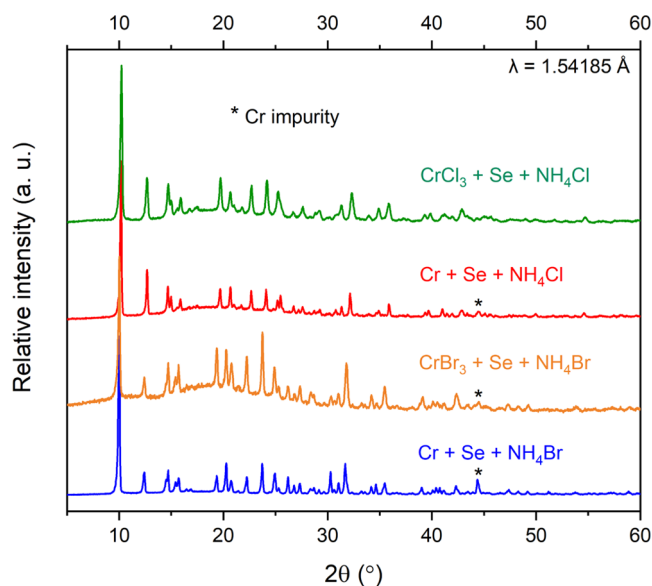


Figure 1. PXRD patterns of $\text{Cr}_2\text{Se}_2(\text{en})_4\text{X}_2$ as synthesized from various reactants.

Argonne National Laboratory using the solvothermal setup reported elsewhere.⁵⁵ Ammonium bromide was dissolved in *en*, which was then injected into the silica capillary containing a stoichiometric mixture of chromium and selenium metal powders. This capillary was pressurized with 40 bar argon to mimic solvothermal conditions. Upon heating, selenium peaks diminish fully at their melting point ~220 °C, above which the chromium metal was the only crystalline phase detected ([Figure S4](#)). No sign of $\text{Cr}_2\text{Se}_2(\text{en})_4\text{Br}_2$ was observed until 290 °C, when a new peak appeared at $2\theta \sim 1.25^\circ$ (outlined in orange), which does not match with the most intense first peak of $\text{Cr}_2\text{Se}_2(\text{en})_4\text{Br}_2$ at $2\theta \sim 1.56^\circ$. Upon further heating to ~340 °C, or cooling back to room temperature, $\text{Cr}_2\text{Se}_2(\text{en})_4\text{Br}_2$ still did not form. Different concentrations of the reagent and the short reaction time used for the *in-situ* experiment are probably the factors that prevent the formation of the $\text{Cr}_2\text{Se}_2(\text{en})_4\text{Br}_2$ dimer compound.

Synthesis of $\text{Cr}_2\text{S}_2(\text{en})_4\text{Cl}_2$. The sulfur analogue, $\text{Cr}_2\text{S}_2(\text{en})_4\text{Cl}_2$, can be obtained in a reaction of stoichiometric ratios of $\text{CrCl}_3 \cdot 6\text{H}_2\text{O}$ with sulfur powder or thiourea in an excess of ethylenediamine under similar solvothermal conditions ([Table S1](#)). The final products of these reactions were polycrystalline powders with no observed crystals suitable for single-crystal X-ray diffraction experiments. The similarities of experimental powder patterns with that of the calculated pattern suggested that the “ $\text{Cr}_2\text{S}_2(\text{en})_4\text{Cl}_2$ ” analogue was formed and was further proved by the shift of peaks to a higher angle ([Figure S5](#)). Rietveld refinement was performed on the high-resolution synchrotron PXRD data to obtain the crystal structure of the Cr_2S_2 dimer ([Figure S6](#)). Both sulfur powder and thiourea used as starting materials can yield phase-pure $\text{Cr}_2\text{S}_2(\text{en})_4\text{Cl}_2$ under the same solvothermal conditions. Irrespective of the chromium starting material used, replacing ammonium chloride with ammonium bromide failed to produce the sulfur bromide analogue of the dimer. This result suggests that the formation of the “ $\text{Cr}_2\text{S}_2(\text{en})_4\text{Br}_2$ ” phase, if exists, is not favored under the mentioned solvothermal conditions.

Synthesis of $\text{Cr}_2\text{Se}_8(\text{en})_4$. This phase was synthesized when $\text{Cr}_2\text{Se}_2(\text{en})_4\text{Br}_2$ was treated with an excess of selenium in

Table 1. Single-Crystal Data Collection and Refinement Parameters for $\text{Cr}_2\text{Se}_2(\text{en})_4\text{Br}_2$, $\text{Cr}_2\text{Se}_2(\text{en})_4\text{Cl}_2$, and $\text{Cr}_2\text{Se}_8(\text{en})_4^a$

	$\text{Cr}_2\text{Se}_2(\text{en})_4\text{Br}_2$	$\text{Cr}_2\text{Se}_2(\text{en})_4\text{Cl}_2$	$\text{Cr}_2\text{Se}_2(\text{en})_4\text{Cl}_2$	$\text{Cr}_2\text{Se}_8(\text{en})_4$
CSD-number	2144990	2144978	2144988	2144989
specimen type	single crystal	single crystal	powder	single crystal
temperature (K)	100(2)			
source	Mo K_α	Mo K_α	synchrotron	Mo K_α
λ (Å)	0.71073	0.71073	0.45791	0.71073
space group	$P21/n$ (No. 14)			$C2/c$ (No. 15)
a (Å)	6.5052(4)	6.4564(8)	6.2859(7)	27.0369(2)
b (Å)	11.2771(8)	11.1494(2)	11.1758(1)	8.1586(5)
c (Å)	14.1312(1)	13.8458(2)	13.8681(3)	24.1599(2)
β (deg)	94.494(3)	94.471(3)	94.353(8)	110.438(4)
V (Å ³)	1033.47(1)	993.7(2)	971.42(2)	4993.8(6)
Z	2	2	2	8
form. weight (g mol ⁻¹)	662.15	573.23	479.43	976.09
ρ_{calc} (g cm ⁻³)	2.128	1.916	1.639	2.597
μ (mm ⁻¹)	8.447	5.033		12.545
data/parameters	2383/101	2762/102	28045/78	5771/331
R_1/wR_2	0.033/0.058	0.067/0.105		0.020/0.040
R_{wp}			0.098	
GOF	1.04	1.09	1.64	1.07
diff. peak/hole (e ⁻ Å ⁻³)	0.88/−0.60	1.15/−1.36		1.18/−0.49

^aFor $\text{Cr}_2\text{Se}_2(\text{en})_4\text{Cl}_2$, Rietveld Refinement was Performed against PXRD Data Collected at 100 K on Beamline 11-BM-B at the APS ANL. Further details of the crystal structure determination may be obtained from Fachinformationszentrum Karlsruhe, Germany, by quoting the CSD depository numbers given in this Table.

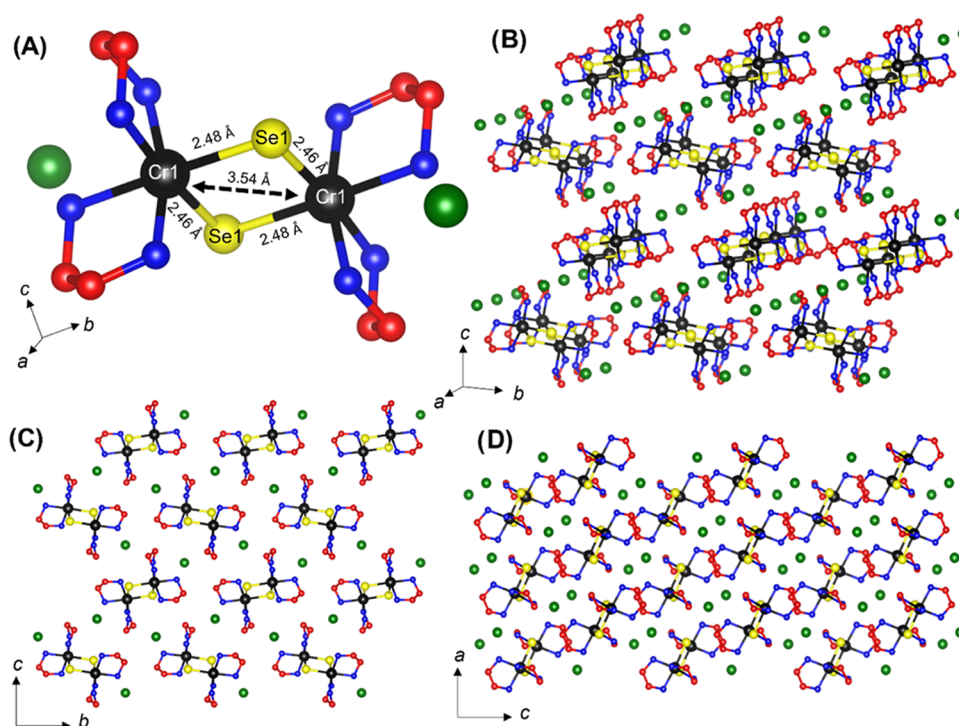


Figure 2. Crystal structure of the $\text{Cr}_2\text{Se}_2(\text{en})_4\text{Cl}_2$ dimer phase. (A) Structure of one dimer fragment. (B) General view along the [100] direction. (C), (D) Views along different crystallographic directions. Cr: black; Se: yellow; N: blue; C: red; and Cl: green. All hydrogen atoms are omitted for clarity.

attempt to eliminate leftover chromium metal in the products. A gradual increase in the amount of selenium gives a mixture of $\text{Cr}_2\text{Se}_2(\text{en})_4\text{Br}_2$ and $\text{Cr}_2\text{Se}_8(\text{en})_4$ until it reaches the stoichiometric ratio giving $\text{Cr}_2\text{Se}_8(\text{en})_4$ with no admixtures (Table S1). Slight differences in the intensities of peaks in experimental and theoretical PXRD patterns could still be observed (Figure S7). Shiny black crystal chunks were visible to the naked eye

and the clusters could be broken up with a needle to isolate the individual crystals. An addition of NH_4Br to this reaction suppresses the formation of $\text{Cr}_2\text{Se}_8(\text{en})_4$ while favoring the recrystallization of the starting material $\text{Cr}_2\text{Se}_2(\text{en})_4\text{Br}_2$. The post-synthetic second treatment of finely ground $\text{Cr}_2\text{Se}_8(\text{en})_4$ with *en* leaves the compound unchanged. Contradictory to the report of Dehnen et al.,⁵⁴ this reaction scheme yields very

stable products that do not decompose under normal atmospheric conditions and it was not necessary to use inert conditions for the synthesis. Even though $\text{Cr}_2\text{Se}_8(\text{en})_4$ is a neutral molecular compound, solubility studies showed it to be insoluble in nonpolar hexane, acetonitrile, and DMF solvents.

Crystal Structure of $\text{Cr}_2\text{Q}_2(\text{en})_4\text{X}_2$ ($\text{Q} = \text{S}, \text{Se}; \text{X} = \text{Cl}, \text{Br}$). $\text{Cr}_2\text{Q}_2(\text{en})_4\text{X}_2$ compounds crystallize in the monoclinic space group $P21/n$ (Table 1). The unit cell volumes of the three isostructural compounds follow the order of $\text{Cr}_2\text{S}_2(\text{en})_4\text{Cl}_2 < \text{Cr}_2\text{Se}_2(\text{en})_4\text{Cl}_2 < \text{Cr}_2\text{Se}_2(\text{en})_4\text{Br}_2$, in agreement with the ionic radii of constituting elements. The general structure of these dimeric compounds is described using the $\text{Cr}_2\text{Se}_2(\text{en})_4\text{Cl}_2$ dimer as a model. The crystal structure of $\text{Cr}_2\text{Se}_2(\text{en})_4\text{Cl}_2$ consists of discrete molecular entities of a Cr dimer connected by two monoatomic selenium bridges, making a slightly distorted square Cr_2Se_2 core (Figure 2A). The crystal structure of a single unit with the atomic displacement parameters (ADPs) is shown in Figure S8. Cr–Se bond distances vary from 2.460(1) to 2.484(2) Å (Table 2),

Table 2. Selected Bond Distances in the Crystal Structures of $\text{Cr}_2\text{Se}_2(\text{en})_4\text{Cl}_2$, $\text{Cr}_2\text{Se}_2(\text{en})_4\text{Br}_2$, $\text{Cr}_2\text{S}_2(\text{en})_4\text{Cl}_2$, and $\text{Cr}_2\text{Se}_8(\text{en})_4$ Dimers

bond	distance (Å)	bond	distance (Å)
$\text{Cr}_2\text{Se}_2(\text{en})_4\text{Cl}_2$			
Cr1–Cr1	3.540(3)	Cr1–Cr1	5.286(8)
Cr1–Se1	2.460(1)	Cr1–Se1	2.509(6)
Cr1–Se1	2.484(2)	Cr1–Se7	2.505(8)
Cr1–N1	2.108(6)	Cr2–Se4	2.490(7)
Cr1–N2	2.100(7)	Cr2–Se8	2.522(6)
Cr1–N3	2.081(7)	Se1–Se2	2.3672(6)
Cr1–N4	2.151(7)	Se2–Se3	2.340(8)
$\text{Cr}_2\text{Se}_2(\text{en})_4\text{Br}_2$			
Cr1–Cr1	3.538(1)	Se4–Se5	2.358(7)
Cr1–Se1	2.463(6)	Se5–Se6	2.352(6)
Cr1–Se1	2.484(7)	Se7–Se8	2.379(7)
Cr1–N1	2.091(3)	Cr1–N1	2.073(2)
Cr1–N1	2.091(3)	Cr1–N2	2.105(3)
Cr1–N2	2.159(2)	Cr1–N3	2.097(2)
Cr1–N3	2.119(3)	Cr1–N4	2.090(2)
Cr1–N4	2.096(3)	Cr2–N5	2.078(3)
$\text{Cr}_2\text{S}_2(\text{en})_4\text{Cl}_2$			
Cr1–Cr1	3.304(3)	Cr2–N6	2.123(3)
Cr1–S1	2.343(2)	Cr2–N7	2.104(2)
Cr1–S1	2.334(3)	Cr2–N8	2.080(3)
Cr1–N1	2.109(3)		
Cr1–N2	2.115(4)		
Cr1–N3	2.201(4)		
Cr1–N4	2.116(5)		

while Se–Cr–Se and Cr–Se–Cr angles are 88.51(5) and 91.49(5)°, respectively. Cr–Cr bond distance across the core is 3.540(3) Å. Chromium atoms remain six coordinated by bonding to four N atoms from two ethylenediamine ligands. A variation in Cr–N bond distances results in a distorted octahedral geometry (Table 2) and a $\sim C_{2v}$ ($mm2$) local symmetry around chromium. Two accompanying Cl^- anions prompt the dimer cation to have a +2 charge, indicating Cr^{3+} and Se^{2-} oxidation states.

Cr_2Se_2 dimers are stacked along the [100] direction and the charge balancing Cl^- ions are arranged in channels along the same direction (Figure 2B,C). Layers of alternating dimer fragments are arranged in the ABAB sequence (Figure 2C).

The view along the [010] direction shows the Cl^- channels organized in pairs in a diagonal fashion (Figure 2D). Although the dimers have no covalent connection to each other, the crystal structure is stabilized by van der Waals and electrostatic interactions. 3D packing of the discrete units is supported by N–H...Se (2.552 Å) and N–H...Cl (2.440 and 2.613 Å) hydrogen bonding interactions. Single-crystal X-ray diffraction shows that $\text{Cr}_2\text{Se}_2(\text{en})_4\text{Br}_2$ is isostructural to $\text{Cr}_2\text{Se}_2(\text{en})_4\text{Cl}_2$.

The crystal structure for $\text{Cr}_2\text{S}_2(\text{en})_4\text{Cl}_2$ was refined using high-resolution synchrotron PXRD (Figure S6). Rietveld refinement confirmed it to be isostructural to the Se dimers discussed above. The unit cell of the Cr_2S_2 dimer is smaller than its selenium counterpart particularly along the [100] axis due to the smaller atomic radii of sulfur (Table 1). The Cr_2S_2 core is less distorted than that of the Se compound, and Cr–S distances vary from 2.334(3) to 2.343(2) Å, while the Cr–Cr distance across the core is 3.304(3) Å (Table 2). The respective S–Cr–S and Cr–S–Cr angles measure to be 90.08(9) and 89.92(9)° respectively, giving rise to a rather shrunken core. The Cr–N bond distances completing the octahedral geometry range from 2.109(3) to 2.201(4) Å.

Crystal Structure of the $\text{Cr}_2\text{Se}_8(\text{en})_4$ Phase. $\text{Cr}_2\text{Se}_8(\text{en})_4$ crystallizes in the space group $C2/c$; lattice parameters are given in Table 1. Unlike the closed Cr_2Se_2 core of $\text{Cr}_2\text{Se}_2(\text{en})_4\text{X}_2$, Cr atoms in $\text{Cr}_2\text{Se}_8(\text{en})_4$ are connected to each other with one –Se–Se– bridge. Each chromium atom is also connected to an arm of three selenium atoms, –Se–Se–Se, protruding like the claws of a crustacean (Figure 3A). The crystal structure of a single unit with ADPs is shown in Figure S9. Chromium maintains its six coordinated geometry with four N atoms from two ethylenediamine molecules completing the metal coordination. Cr–N bond distances ranging from 2.073(2) to 2.123(3) Å along with varying Cr–Se bonds make the geometry around chromium to be of a distorted octahedron. Every Se–Se bond is different with an average of 2.5 Å (Table 2) so that the selenium arms are not identical. Interatomic bond distance between chromium atoms has increased to 5.286(8) Å due to the extra bridging selenium atom.

The individual fragments are arranged in such a manner that its protruding selenium arms are pointed toward the Cr–en chelate rings of the neighboring fragments (Figure 3B,C). This arrangement creates a pseudo-two-dimensional ladder-like structure where the entwined chains propagate along the [001] direction (Figure 3C). The superficial ladders consist of Cr–Se backbones appearing as rails connected by the selenium arms acting as steps and the “ladders” look well separated from one another. Since $\text{Cr}_2\text{Se}_8(\text{en})_4$ is a neutral molecule, chromium holds a +3 charge, while Se2 and Se5 are neutral, leaving the rest of the Se atoms at a –1 charge.

Magnetic Properties. In the crystal lattices containing the dimeric transition-metal complexes, the intermolecular interactions are typically very weak, precluding long-range magnetic ordering. In turn, the intradimer magnetic coupling can be quite strong resulting in a significant deviation from paramagnetic Curie–Weiss behavior at temperatures when coupling strength is comparable to thermal energy. The strength of the magnetic coupling J depends on the distance between the metal centers as well as on the type of the bridging ligand that may facilitate magnetic superexchange interactions.⁵⁹ Metal dimers with antiferromagnetic coupling exhibit a maximum in their magnetic susceptibility (χ) versus temperature dependence. With increasing antiferromagnetic interaction, the temperature of that maximum increases, while its

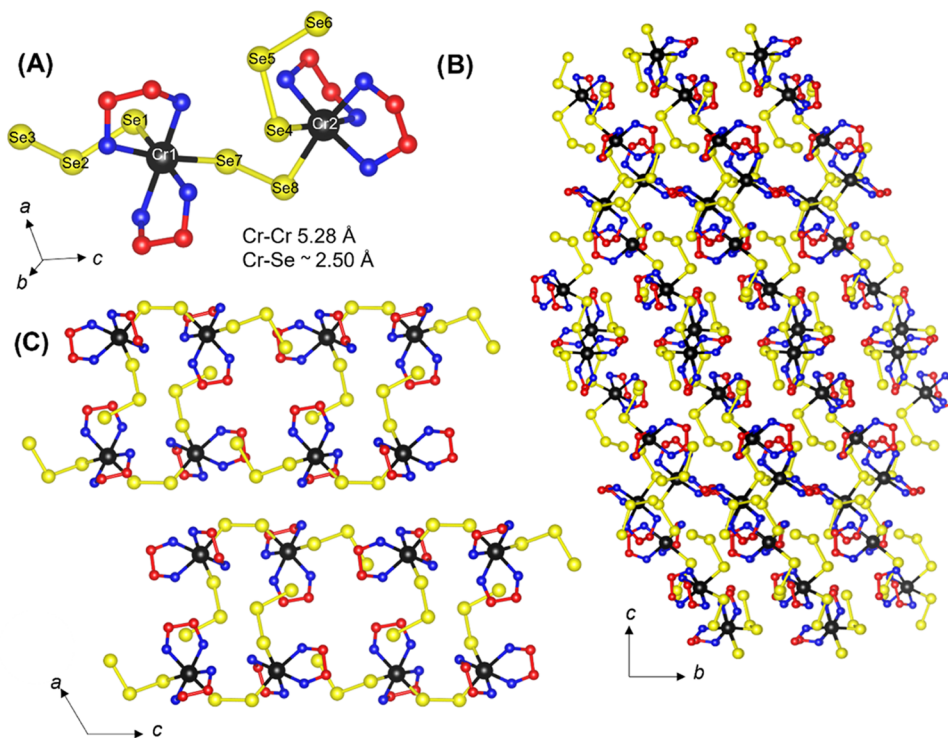


Figure 3. Crystal structure of $\text{Cr}_2\text{Se}_8(\text{en})_4$. (A) Structure of one molecule of $\text{Cr}_2\text{Se}_8(\text{en})_4$. (B, C) General views in the $[100]$ and $[010]$ crystallographic directions. Cr: black; Se: yellow; N: blue; and C: red. All hydrogen atoms are omitted for clarity.

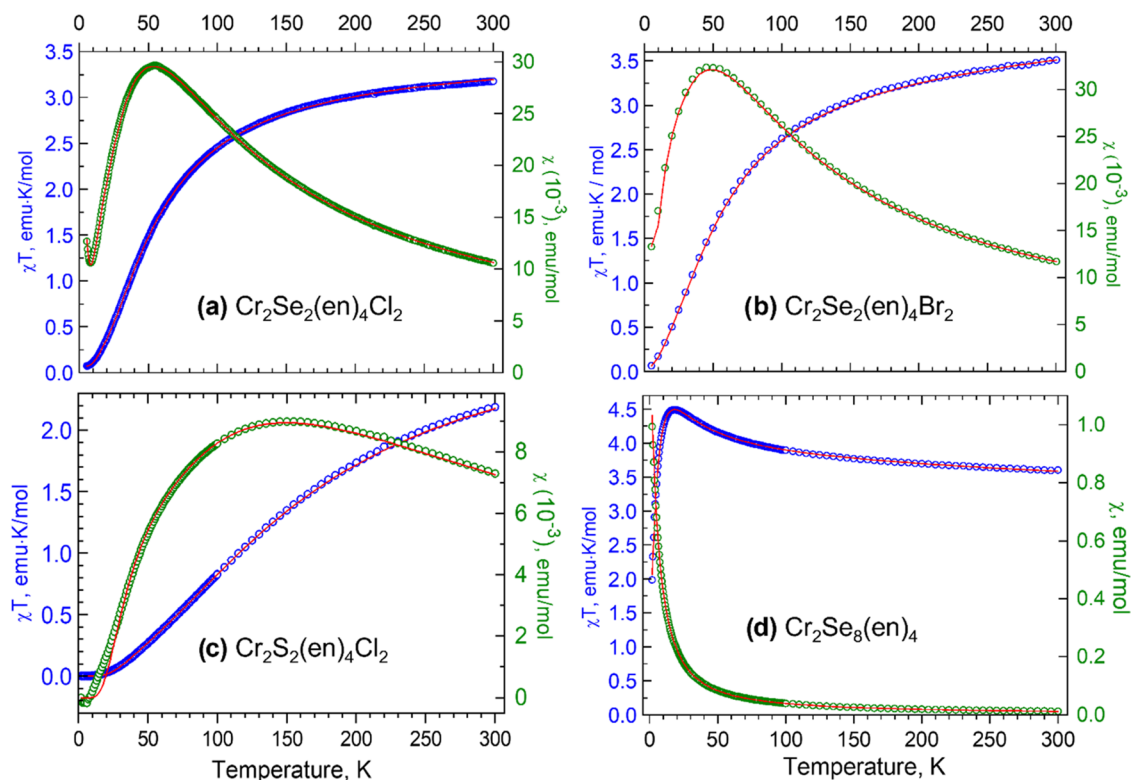


Figure 4. Experimental χ vs T (green) and χT vs T (blue) data measured at the magnetic field of 1000 Oe for (a) $\text{Cr}_2\text{Se}_2(\text{en})_4\text{Cl}_2$, (b) $\text{Cr}_2\text{Se}_2(\text{en})_4\text{Br}_2$, (c) $\text{Cr}_2\text{S}_2(\text{en})_4\text{Cl}_2$, and (d) $\text{Cr}_2\text{Se}_8(\text{en})_4$. The red plots were simulated using a spin Hamiltonian including the biquadratic exchange given in Table 3.

height decreases.^{59–61} Also, the maximum becomes broader with increasing interaction energy. On the other hand,

ferromagnetic dimers show a maximum in their χT vs T dependence.

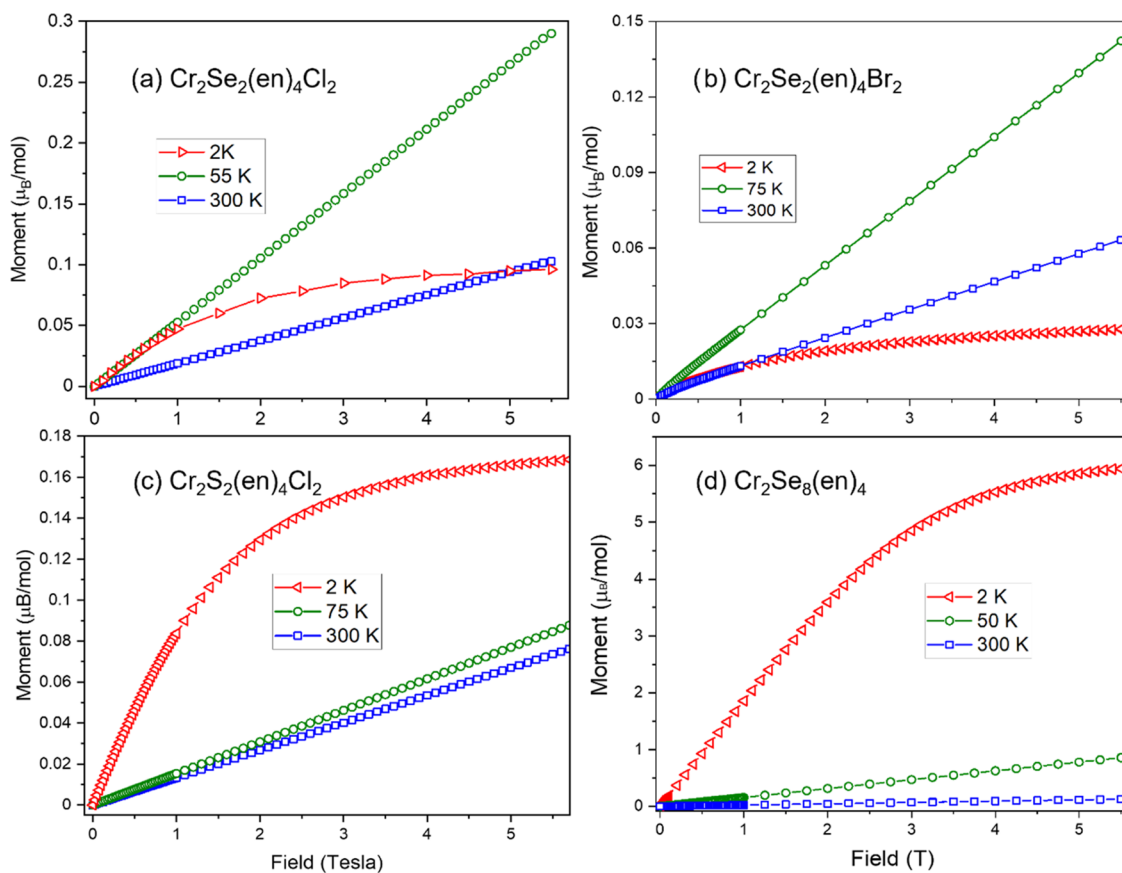


Figure 5. Isothermal magnetization (M vs H) curves for (a) $\text{Cr}_2\text{Se}_2(\text{en})_4\text{Cl}_2$, (b) $\text{Cr}_2\text{Se}_2(\text{en})_4\text{Br}_2$, (c) $\text{Cr}_2\text{S}_2(\text{en})_4\text{Cl}_2$, and (d) $\text{Cr}_2\text{Se}_8(\text{en})_4$ compounds measured at different temperatures.

First, to ensure phase purity of the $\text{Cr}_2\text{Q}_2(\text{en})_4\text{X}_2$ samples, isothermal magnetization, $M(H)$ studies were conducted at 2, 50–75, and 300 K. For all four compounds, $M(H)$ data under an applied field of 0–1.0 T show that the samples are clean of ferro- or ferrimagnetic impurities (Figure S10). Based on this result, magnetic susceptibility measurements were conducted under an applied field of 1000 Oe (Figure 4) to be the linear limit of $M(H)$ even at the lowest temperatures.

The temperature dependence of the magnetic susceptibility of $\text{Cr}_2\text{Se}_2(\text{en})_4\text{Cl}_2$ synthesized from elemental Cr powder suggests the presence of a dimer with moderately strong antiferromagnetic coupling. Similar magnetic properties were observed for the sample of $\text{Cr}_2\text{Se}_2(\text{en})_4\text{Cl}_2$ made from soluble $\text{CrCl}_3 \cdot 6\text{H}_2\text{O}$ with no ferro- or ferrimagnetic impurity. Magnetic characterization of $\text{Cr}_2\text{Se}_2(\text{en})_4\text{Cl}_2$ indicates an antiferromagnetic exchange in the Cr dimer emphasized in the peak in the χ vs T curve around 55 K, with a maximum χ value of $\sim 30 \times 10^{-3}$ emu/mol (note that the scales in the plots are adjusted to clearly show the low-temperature features), followed by a sharp decrease in susceptibility at lower temperatures (Figure 4a). The χT vs T plot exhibits a steady nonlinear decline down to ~ 75 K and a subsequent drop over a short temperature range in accordance with antiferromagnetic interactions in the Cr_2Se_2 dimer (Figure 4a). Isothermal magnetization agrees with the antiferromagnetic coupling where low values of magnetization were observed at 2 K reaching a saturated value of $0.1 \mu_{\text{B}}$ under 6 T (Figure 5a).

Magnetic characterization of $\text{Cr}_2\text{Se}_2(\text{en})_4\text{Br}_2$ demonstrated a similar trend to its chloride counterpart. The χ vs T curve with a maximum value of $\sim 32 \times 10^{-3}$ emu/mol at 45 K (Figure 4b)

is characteristic of antiferromagnetic coupling and displays a nonlinear decrease with a decreasing temperature (Figure 4b). Isothermal magnetization displays the lowest values of magnetization at 2 K (Figure 5b).

Magnetic studies for $\text{Cr}_2\text{S}_2(\text{en})_4\text{Cl}_2$ were conducted on samples synthesized from $\text{CrCl}_3 \cdot 6\text{H}_2\text{O}$ and thiourea. Overall susceptibility and magnetization for the $\text{Cr}_2\text{S}_2(\text{en})_4\text{Cl}_2$ dimer are significantly lower compared to the $\text{Cr}_2\text{Se}_2(\text{en})_4\text{X}_2$ dimers. The χ vs T plot displayed a broad maximum centered around 150 K indicating strong antiferromagnetic coupling between Cr centers followed by a steady reduction in susceptibility down to 5 K (Figure 4c). The maximum χ value of $\sim 9.0 \times 10^{-3}$ emu/mol is only 1/3 of the maximum χ of the selenium analogue. It is important to note that the onset of the broad maximum takes place at a higher temperature for Cr_2S_2 dimers than that for both Cr_2Se_2 dimers. The χT vs T plot shows a gradual nonlinear decrease with decreasing temperatures, which is typical for antiferromagnetically coupled dimers (Figure 4c). Isothermal magnetization is at a maximum of 2 K and reaches saturation of $0.2 \mu_{\text{B}}$ under 6 T (Figure 5c).

For $\text{Cr}_2\text{Se}_8(\text{en})_4$, finely ground crystal chunks handpicked from the sample were used for magnetic studies. Magnetic susceptibility shows no magnetic ordering down to 1.8 K under 1000 Oe applied field (Figure 4d). The increasing χT product with a maximum of ~ 30 K upon cooling indicates ferromagnetic interactions between Cr atoms connected by the Se_2 bridge (Figure 4d). A sharp drop in χT values below 18 K is due to the weak antiferromagnetic interaction between the dimer molecules. The field dependence of magnetization confirms the ferromagnetic nature of the Cr–Cr interactions;

Table 3. Spin Hamiltonian Parameters Found from the Magnetic and HF-EPR Data^a

complex	magnetism data			HF-EPR data					
	J (cm ⁻¹)	j (cm ⁻¹)	g_x	g_y	g_z	D (cm ⁻¹)	E (cm ⁻¹)	D_{Cr} (cm ⁻¹)	E_{Cr} (cm ⁻¹)
Cr ₂ Se ₂ (en) ₄ Cl ₂	15.1 (3.54 Å)	2.1	1.993	1.993	2.002	1.019 ^b	0.112 ^b	-0.4	0.0
Cr ₂ Se ₂ (en) ₄ Br ₂	17.7 (3.54 Å)	1.0	1.993	1.993	2.003	1.05 ^b	0.159 ^b	-0.4	-0.02
Cr ₂ S ₂ (en) ₄ Cl ₂	49.0 (3.30 Å)	4.6	1.991	1.991	1.989	0.340 ^b	0.075 ^b	-0.09	0.02
Cr ₂ Se ₈ (en) ₄	-6.1 (5.27 Å)	0.85	1.997	2.00	1.975	0.046 ^c	0.0075 ^c		

^aThe Cr–Cr bond distances are indicated in parentheses. J : exchange constant, j : biquadratic exchange constant, g_x, g_y, g_z : g -factor components, D and E : contribution to zero-field splitting caused by the anisotropic metal–metal interactions, and D_{Cr}, E_{Cr} : zero-field splitting on each d^3 ion. ^bParameters in the $S = 1$ state. ^cParameters in the $S = 3$ state. The estimated errors are few units in the last reported digit.

the highest magnetization was observed at the lowest temperature, 2 K (Figure Sd). At the applied magnetic field of 5.5 T, the saturation magnetization of 6 μ_B /f.u. was achieved as expected for two Cr³⁺ ions with aligned spins.

Magnetic Exchange Calculations. Exchange interactions between two Cr³⁺ ions with spin $S = 3/2$ give rise to four states of coupled spin $\hat{S} = \hat{S}_1 + \hat{S}_2$, with the total S quantum numbers 0, 1, 2, and 3.^{8,11,34–45,59–64} The magnetic properties of such dimeric systems are usually described by the Heisenberg–Dirac–VanVleck (HDVV) Hamiltonian

$$H = J\hat{S}_1 \cdot \hat{S}_2 \quad (1)$$

where \hat{S}_1 and \hat{S}_2 are the spin operators on centers 1 and 2. A positive J corresponds in this notation to antiferromagnetic interactions. (Note that other notations have also been used in the literature, like $-J\hat{S}_1 \cdot \hat{S}_2$ and $-2J\hat{S}_1 \cdot \hat{S}_2$). In our case, attempts of fitting the magnetic susceptibility by using energies resulting from eq 1 were unsuccessful indicating a need for the inclusion of the biquadratic exchange term $j(\hat{S}_1 \cdot \hat{S}_2)^2$. Interestingly, the need to include the biquadratic exchange often arises in studies on coupled Cr³⁺ pairs,^{35,36,38,40,45,62–66} while this term may not be needed in other d^3 – d^3 dimers.⁸ It is associated with the effect of the exchange interaction on the metal–metal distance and is correlated with the elastic stiffness coefficient.⁶⁵ This is referred to as the “exchange striction” and is expected to produce positive j values in the notation used in this paper.⁶⁵ (Note that ref 65 uses a different sign convention) This effect is particularly strong in the case of Cr dimers having 90° Cr–X–Cr bridges,⁶⁵ like in Cr₂X₂ cores reported here. The effects of the biquadratic exchange on two-dimensional magnets have been investigated recently.⁶⁶

The corrected spin Hamiltonian is

$$\hat{H} = J\hat{S}_1 \cdot \hat{S}_2 - j(\hat{S}_1 \cdot \hat{S}_2)^2 \quad (1a)$$

The magnetic susceptibility per one mole of the dimer can be calculated from

$$\chi = \frac{N\mu_B^2 g^2}{3k_B T} \frac{\sum_{S=0}^3 (2S+1)(S+1)S \exp\left(-\frac{E_S}{k_B T}\right)}{\sum_{S=0}^3 (2S+1) \exp\left(-\frac{E_S}{k_B T}\right)} + 2\text{TIP} \quad (2)$$

In (2), the energies E_S calculated according to either spin Hamiltonian (1) or (1a) can be used (TIP: temperature-independent parameter). This method works well provided that the energy splits within the S states are small compared to the thermal energy, $k_B T$. In our cases, the zero-field splitting effects are small (see below), and the approach described above should work properly. At high fields, the Zeeman splitting becomes comparable to or larger than the thermal

energy at low temperatures. To account for such effects, a full “microscopic” spin Hamiltonian (3) was used.

$$\begin{aligned} \hat{H} = & J\hat{S}_1 \cdot \hat{S}_2 - j(\hat{S}_1 \cdot \hat{S}_2)^2 + \mu_B B \{g_x \hat{S}_1 + g_y \hat{S}_2\} \\ & + D_{Cr} \left\{ \hat{S}_{z1}^2 - \frac{1}{3} S(S+1) \right\} + E_{Cr} (\hat{S}_{x1}^2 - \hat{S}_{y1}^2) \\ & + D_{Cr} \left\{ \hat{S}_{z2}^2 - \frac{1}{3} S(S+1) \right\} + E_{Cr} (\hat{S}_{x2}^2 - \hat{S}_{y2}^2) \\ & + D_{12} \left\{ \hat{S}_{z1} \hat{S}_{z2} - \frac{1}{3} \hat{S}_1 \cdot \hat{S}_2 \right\} + E_{12} (\hat{S}_{x1} \hat{S}_{x2} - \hat{S}_{y1} \hat{S}_{y2}) \end{aligned} \quad (3)$$

Parameters D_{Cr} and E_{Cr} describe the zero-field splitting on each d^3 ion, while D_{12} and E_{12} describe the contribution to zero-field splitting caused by the anisotropic metal–metal interactions. The reported here dimeric dimers are centrosymmetric and using the same D_{Cr} and E_{Cr} for both atoms is justified. Although this is not true for the ferromagnetic monobridged complex, the same approach was used since there is no way to determine these parameters separately for each ion. The spin Hamiltonian (3) operates within the set of 16 lm_{S1}, m_{S2} functions in a d^3 – d^3 dimer. The energy levels in the magnetic fields calculated using spin Hamiltonian (3) are presented in Figure S11. To calculate the magnetic susceptibility, the fundamental equation employed was

$$\chi_{\text{dim}} = -\frac{N_A}{B} \frac{\sum_i \frac{\partial E_i}{\partial B} \exp\left(-\frac{E_i}{kT}\right)}{\sum_i \exp\left(-\frac{E_i}{kT}\right)} + 2\text{TIP} \quad (4)$$

The 16 energies E_i were calculated by diagonalizing spin Hamiltonian (3). The derivatives with respect to the magnetic field B , $\frac{\partial E_i}{\partial B}$, were evaluated by calculating the energies 5 Gauss below and 5 Gauss above the applied field of the SQUID magnetometer. Trace paramagnetic contamination present in the antiferromagnetic dimers was considered by modifying eq 4

$$\chi = (1-x)\chi_{\text{dim}} + 2x \frac{N\mu_B^2 g^2}{3k_B T} \frac{15}{4} \quad (5)$$

where x is the fraction of a $S = 3/2$ impurity. Finally, the susceptibility was corrected for the interactions with neighboring dimers, zJ , as

$$\chi_{\text{corr}} = \frac{\chi}{1 - \chi z J / N\mu_B^2 g^2} \quad (6)$$

χ_{corr} of eq 6 was fitted to the experimental data. Parameters D_{Cr} were fixed to the values found from EPR. Parameters $E_{Cr}, D_{12},$

and E_{12} were neglected in calculating the magnetic susceptibility.

The magnetic fitting results are presented in Table 3 together with the HF-EPR results. All three dibridged dimers exhibit antiferromagnetic interactions, while the single-bridged complex $\text{Cr}_2\text{Se}_8(\text{en})_4$ is ferromagnetic. The biquadratic exchange constants are positive with magnitudes ranging from ~ 6 to $\sim 14\%$ of the respective J values.

High-field EPR Spectra. The spin Hamiltonian parameters can in principle be determined in each coupled spin state, as was done in ref 45. Unfortunately, the spectra observed in this work did not contain as much information. $\text{Cr}_2\text{Se}_2(\text{en})_4\text{Cl}_2$ produced the best EPR spectra in this series. A characteristic pattern of signals due to the coupled spin state $S = 1$, with a prominent “forbidden” $\Delta M_S = 2$ transition, could be observed over a narrow temperature range and was best seen at 10 K (Figures 6 and 7).

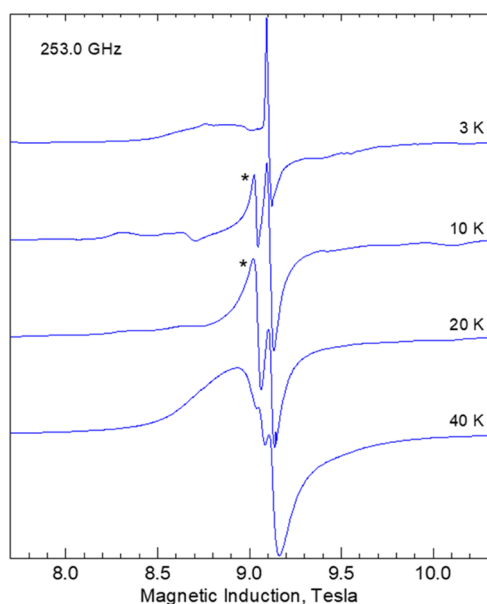


Figure 6. Temperature dependence of the $\Delta M_S = 1$ signals in the 253 GHz spectra of $\text{Cr}_2\text{Se}_2(\text{en})_4\text{Cl}_2$. The asterisk indicates a possible resonance in the $S = 2$ state. The sharp central feature located at $g = 1.985$ is probably due to a monomeric Cr^{3+} impurity. See also Figures 7, S11, and S12.

At temperatures above 30 K (Figure 6), only a broad signal was observed presumably as a result of fast relaxation between the coupled spin states of $S = 1, 2$, and 3 of the dimer. At 20 and 10 K, the $S = 2$ and $S = 1$ signals are visible, and their relative intensities change with temperature according to the population of these states, thus the $S = 2$ signal disappears faster than the $S = 1$ signal when lowering the temperature (Figure S12). No resonances due to the $S = 3$ state could be observed owing to the low population of this state. Both the $S = 1$ and $S = 2$ signals are not seen at 3 K. The resonances still observed at 3 K cannot therefore be due to the antiferromagnetic dimer. The signal marked with an asterisk in Figure 6 may belong to the $S = 2$ spectrum, but no other $S = 2$ or $S = 3$ resonances could be identified. This made an experimental determination of the spin Hamiltonian parameters of $S = 2$ and $S = 3$ states impossible, and the spin Hamiltonian parameters of only the triplet state ($S = 1$) could be determined. The “giant spin” Hamiltonian used was

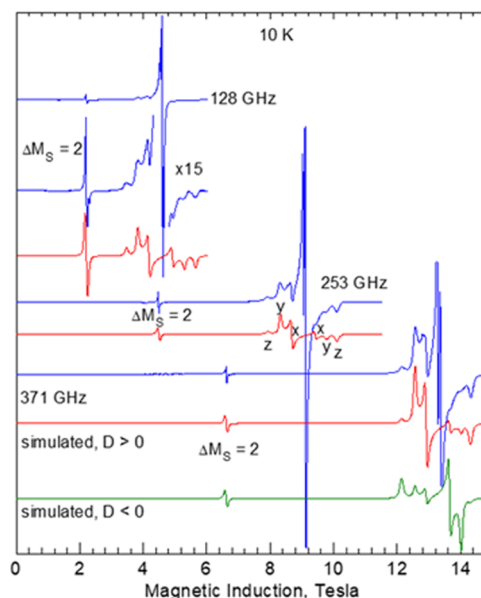


Figure 7. HF-EPR spectra of $\text{Cr}_2\text{Se}_2(\text{en})_4\text{Cl}_2$ recorded at 10 K with microwave frequencies as shown. Labels x , y , and z designate the orientation of the molecule versus the magnetic field at which these transitions occur. The “forbidden” $\Delta M_S = 2$ feature is marked. The red traces were simulated for $S = 1$ with parameters in Table 3 ($D, E > 0$) and the green trace at the bottom was simulated with D and E of the same magnitude but assumed negative to illustrate the effect of the sign of D .

$$\hat{H}_S = \mu_B \mathbf{B} \{ \mathbf{g}_S \} \hat{\mathbf{S}} + D_S \left\{ \hat{S}_z^2 - \frac{1}{3} S(S+1) \right\} + E_S (\hat{S}_x^2 - \hat{S}_y^2) \quad (7)$$

Parameters D_S and E_S are different in different coupled spin states (that is $S = 1, 2$, and 3) of a dimer. These parameters contain contributions due to zero-field splitting on separate $S = 3/2$ ions (D_{Cr} , E_{Cr}) and contributions due to the anisotropic interactions between the ions (D_{12} , E_{12}). In a d^3-d^3 dimer case, the relations between the parameters of the “giant spin” Hamiltonian (7) and the “microscopic” Hamiltonian (3) are^{8,11,36,40,43,45}

$$\begin{aligned} D_{S=1} &= 1.7 D_{12} - 2.4 D_{\text{Cr}} \\ D_{S=2} &= 0.5 D_{12} \\ D_{S=3} &= 0.3 D_{12} + 0.4 D_{\text{Cr}} \end{aligned} \quad (8)$$

The same coefficients relate the coupled-spin E_S parameters to E_{12} and E_{Cr} , and the limitations of this model were discussed recently.⁴⁰

Spectra shown as red traces in Figure 7 were simulated using $S = 1$, $g_x = 1.993$, $g_y = 1.993$, $g_z = 2.002$, $D_{S=1} = 1.019 \text{ cm}^{-1}$, and $E_{S=1} = 0.112 \text{ cm}^{-1}$. The intensity pattern with the high-field “ z ” features being stronger than the low-field “ z ” features, particularly at the highest frequency, while the high-field “ x ” and “ y ” features are weaker than their low-field partners is consistent with positive $D_{S=1}$ (Figure 7).

Since we know only the parameters of the $S = 1$ state, the determination of D_{Cr} , D_{12} , and E_{Cr} , E_{12} cannot be accomplished experimentally. The D_{12} parameter is expected to consist mainly of the magnetic dipole–dipole interaction between the Cr^{3+} ions

$$D_{12} = -\frac{3\mu_B^2 g^2}{R^3} \quad (9)$$

where R is the distance between ions. The dipolar contribution to E_{12} is expected to be zero due to very small g anisotropy. With $R = 3.54$ Å, for both $\text{Cr}_2\text{Se}_2(\text{en})_4\text{Cl}_2$ and $\text{Cr}_2\text{Se}_2(\text{en})_4\text{Br}_2$, one obtains D_{12} of -0.12 cm^{-1} . In turn, $D_{S=2}$ of around -0.06 cm^{-1} is expected according to eq 8. This is a high estimate because the electron delocalization, which is not considered in eq 9, will result in the reduction of the dipole–dipole contribution to D_{12} . Eq 9 produces a D_{12} equal to -0.14 cm^{-1} for $\text{Cr}_2\text{S}_2(\text{en})_4\text{Cl}_2$ ($R = 3.3$ Å). For the three centrosymmetric dimers $\text{Cr}_2\text{Se}_2(\text{en})_4\text{Cl}_2$, $\text{Cr}_2\text{Se}_2(\text{en})_4\text{Br}_2$, and $\text{Cr}_2\text{S}_2(\text{en})_4\text{Cl}_2$, the “ Z ” axis of the D_{Cr} tensor is expected to be approximately perpendicular to the Cr_2X_2 plane, while the “ Z ” axis of the dipolar D_{12} tensor is along the $\text{Cr}-\text{Cr}$ direction. To apply eq 8, to estimate D_{Cr} and E_{Cr} the D_{Cr} and D_{12} tensors must be expressed in the same coordinates, which can be accomplished by rotating the D_{12} tensor by 90° about an axis lying in the Cr_2X_2 plane and perpendicular to the $\text{Cr}-\text{Cr}$ vector. When doing so, the $D_{12} = -0.12$ cm^{-1} and $E_{12} = 0$ parameter calculated above convert to $D_{12} = 0.06$ cm^{-1} and $E_{12} = -0.06$ cm^{-1} . The D_{Cr} and E_{Cr} values in Table 3 were obtained from these latter D_{12} , E_{12} , as well as from $D_{S=1}$, $E_{S=1}$. For $\text{Cr}_2\text{Se}_8(\text{en})_4$ with the $\text{Cr}-\text{Cr}$ distance of 5.27 Å, eq 9 produces D_{12} of -0.035 cm^{-1} . This is however a noncentrosymmetric system, possibly with different z fs parameters on each Cr^{3+} ion, and the simple procedure described above cannot be applied. We therefore do not attempt to estimate D_{Cr} and E_{Cr} in this case. A more in-depth description of that procedure can be found in refs 8, 45.

$\text{Cr}_2\text{Se}_2(\text{en})_4\text{Br}_2$ produced spectra very similar to those of $\text{Cr}_2\text{Se}_2(\text{en})_4\text{Cl}_2$ (Figure 8). Using the “giant spin” approach, as

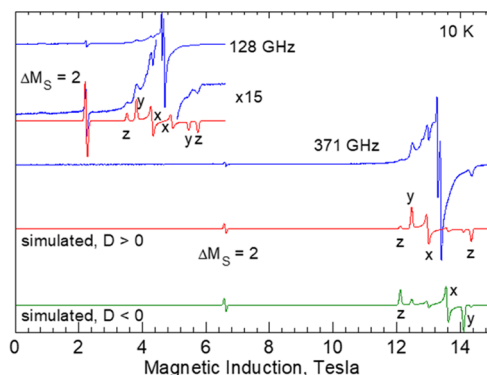


Figure 8. HF-EPR spectra of $\text{Cr}_2\text{Se}_2(\text{en})_4\text{Br}_2$ recorded at 10 K with microwave frequencies as shown. Labels x , y , and z designate the orientation of the molecule versus the magnetic field at which these transitions occur. The “forbidden” $\Delta M_S = 2$ feature is marked. The red traces were simulated for $S = 1$ with parameters in Table 3 (D , $E > 0$) and the green trace at the bottom was simulated with D and E negative, resulting in an incorrect intensity pattern.

above, the following spin Hamiltonian parameters were found: $g_x = 1.993$, $g_y = 1.993$, $g_z = 2.003$, $D_{S=1} = 1.047$ cm^{-1} , and $E_{S=1} = 0.159$ cm^{-1} . The main difference compared to $\text{Cr}_2\text{Se}_2(\text{en})_4\text{Cl}_2$ is a considerably larger E value in the Br species (by a factor of 1.4), resulting in larger spacing between the X and Y features, as seen when Figure 7 is compared to Figure 8.

We cannot offer a justification for that difference in E , as the environment of the Cr^{3+} ions and the distance between them are similar in both complexes. The parameters may be affected by the presence of the heavy Br atom with stronger spin–orbit coupling, even if Br is not coordinated to Cr. Similarly, as in $\text{Cr}_2\text{Se}_2(\text{en})_4\text{Cl}_2$, only one feature that may belong to the $S = 2$ state is observed.

$\text{Cr}_2\text{S}_2(\text{en})_4\text{Cl}_2$ spectra are of much lower quality than those of the Se dimers (Figure 9). The $S = 1$ spectrum can be

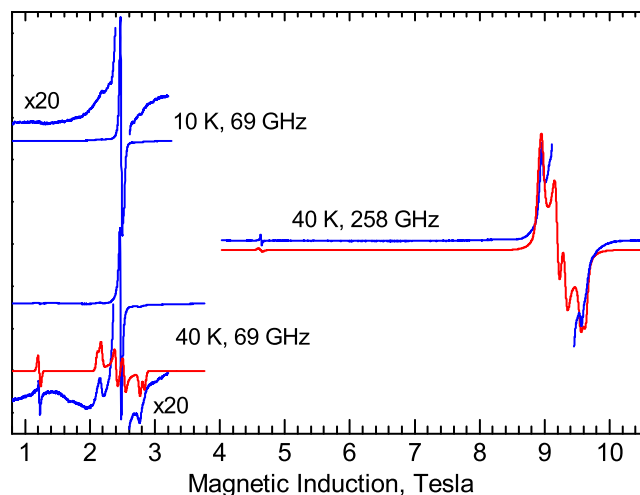


Figure 9. HF-EPR spectra of $\text{Cr}_2\text{S}_2(\text{en})_4\text{Cl}_2$. The “forbidden” $\Delta M_S = 2$ feature is located in the 40 K spectra at 1.22 and 4.63 T, at 69 GHz and at 258 GHz, respectively. The red traces were simulated with parameters in Table 3. A strong central line, which is due to contaminations, was cut off in the 258 GHz plot.

recognized with the $D_{S=1}$ parameter surprisingly much lower than in the Se-bridged compounds. The half-field transition is seen at any microwave frequency, and its position as well as the positions of the “allowed” transitions in the spectra center can be reproduced using $D_{S=1}$ of 0.34 cm^{-1} and $E_{S=1} = 0.075$ cm^{-1} . A contamination probably with monomeric Cr^{3+} species is seen at low temperatures (10 K and below) at which the dimer spectrum disappears due to relatively strong antiferromagnetic exchange interactions.

$\text{Cr}_2\text{Se}_8(\text{en})_4$. The compound exhibits unusually strong relaxation so spectra taken at 3 K are significantly different from those taken at 5 K (Figure 10). With increasing temperature, the outer spectral features move toward the center. Since the complex is ferromagnetic, one should expect an $S = 3$ spectrum at the lowest temperatures. The salient features of the spectra could be tentatively simulated using $S = 3$ and parameters in Table 3, which were determined from the 3 K spectrum. Moreover, an additional weak feature, marked with an asterisk in Figure 11, was seen. That weak feature was observed at a frequency-independent distance from the main spectrum (Figure 11). The frequency dependence of that resonance allowed us to determine a g value of 1.975. Integration of the spectra (not shown) indicates that this feature has a very low intensity compared to the main spectrum.

Theoretical Calculations. “Broken symmetry” DFT calculations^{67–72} were performed to get insights into the metal–metal interactions in the dimers studied here. We have used the free software package ORCA 5.01.⁷³ DFT calculations used the B3LYP/G, functional in combination with the ma-

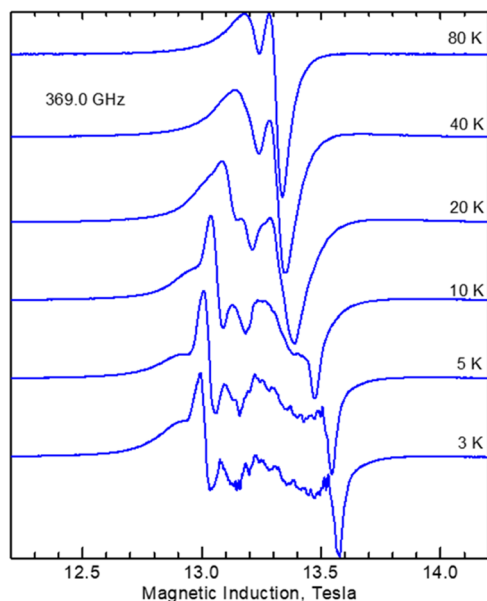


Figure 10. The temperature dependence of the HF-EPR spectra of $\text{Cr}_2\text{Se}_8(\text{en})_4$.

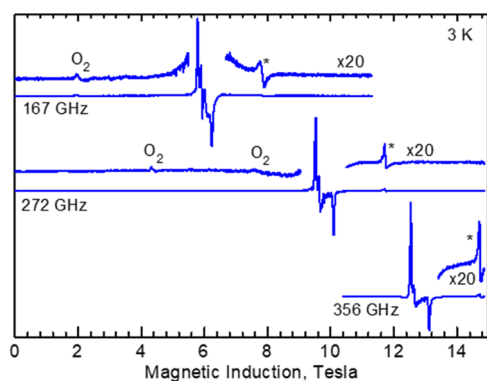


Figure 11. HF-EPR spectra of $\text{Cr}_2\text{Se}_8(\text{en})_4$ recorded at 3 K and frequencies indicated. Signals due to adsorbed oxygen on the powder sample are marked with O_2 , and the additional signals are marked with * in the magnified spectra.

def2-TZVPP function basis for all atoms. “Broken symmetry” first performs an SCF calculation for a high-spin state (HS, with $S = 3$), with three spin-up electrons on one metal atom in a dimer and three spin-up electrons on another metal atom. Next, another SCF calculation is done with three spin-up electrons on one atom and three spin-down electrons on another. This is referred to as a “broken symmetry” state (BS). The J values of the $\hat{H} = J\hat{S}_1\hat{S}_2$ Hamiltonian are then evaluated from the energies of the HS and BS states as $J = 2(E_{\text{HS}} - E_{\text{BS}}) / (\langle \hat{S}^2 \rangle_{\text{HS}} - \langle \hat{S}^2 \rangle_{\text{BS}})$, where $\langle \hat{S}^2 \rangle$ are the average values of the total spin-squared operator in the respective states. It has been reported that the J values derived from such calculations tend to be too large, which is thought to be due to “self-interaction errors” inherent to DFT.^{68,69} An empirical divisor of 2 has often been applied in the literature.^{68,69} The calculated J values reported below have been corrected using this factor.

The J values of 10.6, 12.6, 44.0, and -14.3 cm^{-1} were obtained for $\text{Cr}_2\text{Se}_2(\text{en})_4\text{Cl}_2$, $\text{Cr}_2\text{Se}_2(\text{en})_4\text{Br}_2$, $\text{Cr}_2\text{S}_2(\text{en})_4\text{Cl}_2$, and $\text{Cr}_2\text{Se}_8(\text{en})_4$, respectively. When compared to the experimental magnitudes (15.1, 17.7, 49.0, and -6.1 cm^{-1}), extracted from the magnetic data, one can see that the success

is rather moderate, particularly in the case of $\text{Cr}_2\text{Se}_8(\text{en})_4$. The trends in magnitude and sign of J were properly reproduced, but the quantitative agreement is poor. This problem may be due to the presence of heavy bridging atoms. The antiferromagnetic character of the exchange interaction depends on the overlap of the magnetic orbitals of two ions. The magnetic orbitals and their overlap integrals are shown in Figures 12 and 13. The orbital plots for the Se- and S-bridged

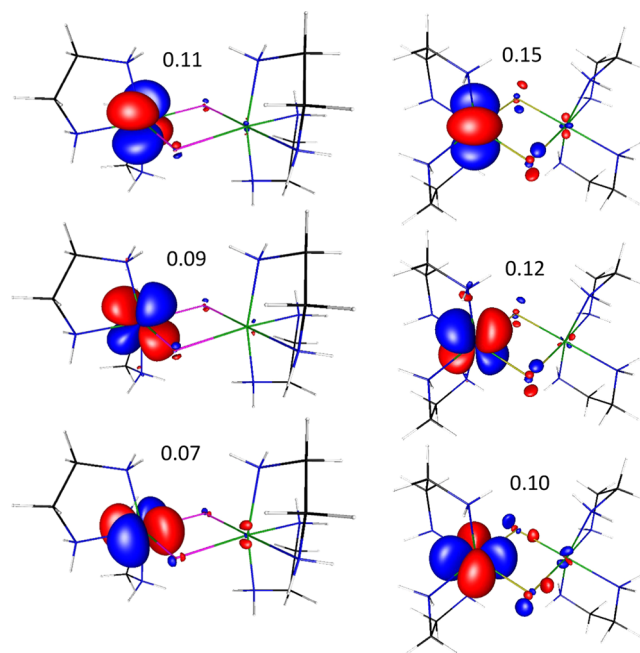


Figure 12. Magnetic orbitals (“corresponding orbitals”, “uco” in the ORCA software) in $\text{Cr}_2\text{Se}_2(\text{en})_4^{2+}$ (left) and $\text{Cr}_2\text{S}_2(\text{en})_4^{2+}$ (right). Note that identical magnetic orbitals exist on the other Cr^{3+} ion in each case. The orbitals are shown at the 0.04 isosurface value. The overlap integrals of the plotted orbitals with their partners located on another Cr^{3+} ion are indicated.

complexes reveal the overall stronger delocalization of the Cr orbitals onto the S bridge than onto the Se bridge and larger overlap integrals of the magnetic orbitals in the S case, leading to much stronger antiferromagnetic exchange in the S-bridged species (Figure 12). This explains the reason behind generally low χ values observed for the Cr_2S_2 dimer when compared to that of Cr_2Se_2 dimers in their respective χ vs T plots.

The $\text{Cr}_2\text{Se}_8(\text{en})_4$ complex is not comparable to the other ones because of the different bridge geometry. The delocalization of the magnetic orbitals onto the bridging Se atoms is very small compared to the cases above (Figure 13). A weak overlap of the magnetic orbitals, one order of magnitude smaller than in the $[\text{Cr}_2\text{Q}_2(\text{en})_4]^{2+}$ species, results in weak ferromagnetic exchange interactions.

An attempt was also made to calculate the ZFS parameters (D_{Cr} , E_{Cr}) of the local quartet ground states using the state-averaged CASSCF method as implemented in the ORCA software.^{74–76} The calculations used the B3LYP/G functional and def2-TZVPP function basis augmented by the def2-TZVPP/C diffuse functions and were performed on molecules in which one of the Cr^{3+} ions was substituted by the diamagnetic Ga^{3+} ion. These calculations were unsuccessful, possibly because of the heavy atoms present in our systems, failing to predict both the magnitude of D and its trend in the

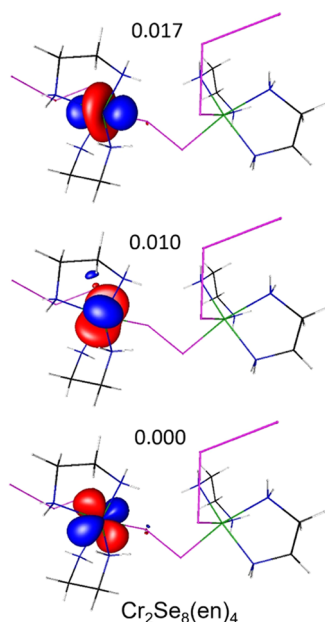


Figure 13. Magnetic orbitals in $\text{Cr}_2\text{Se}_8(\text{en})_4$. Note that identical magnetic orbitals exist on the other Cr^{3+} ion in each case. The orbitals are shown at the 0.04 isosurface value. The overlap integrals are indicated.

Se-bridged versus the S-bridged complexes and will therefore not be described in detail here.

CONCLUSIONS

$\text{Cr}_2\text{Q}_2(\text{en})_4\text{X}_2$ (Q: S, Se; X: Br, Cl; en: ethylenediamine) dimer compounds have been synthesized by low-temperature solvothermal synthesis free from any oxygen-containing ligands or reducing agents. The Se bridges connecting the Cr(III) ions in the Cr_2Se_2 square core mediate magnetic exchange between the metal centers and give rise to moderate (Cr_2Se_2 core) or strong (Cr_2S_2 core) antiferromagnetic interactions. Substituting Se for S resulted in a shorter Cr–Cr separation in the dimer and a significant increase in the strength of magnetic coupling, preserving the antiferromagnetic type of interactions as revealed by magnetic and EPR studies. Finally, replacing monoatomic Se bridges with the diatomic Se–Se bridge in the structure of neutral $\text{Cr}_2\text{Se}_8(\text{en})_4$ resulted in altering the type of exchange from antiferromagnetic to ferromagnetic one. The biquadratic exchange effects were observed. The sign of the biquadratic exchange constant j suggests that this interaction is due to the exchange striction effects.⁶⁵ Reported zero-dimensional dimers are important as discrete molecular building blocks that can be used to form extended structures with tunable magnetic properties.

ASSOCIATED CONTENT

Supporting Information

The Supporting Information is available free of charge at <https://pubs.acs.org/doi/10.1021/acs.inorgchem.2c00298>.

SEM and optical images, table containing a list of synthesis reactions, experimental and theoretical PXRD patterns, 17-BM contour plots, Rietveld refinement data, crystal structures showing ADP and isothermal magnetization curves are included (PDF)

Accession Codes

CCDC 2144978 and 2144988–2144990 contain the supplementary crystallographic data for this paper. These data can be obtained free of charge via www.ccdc.cam.ac.uk/data_request/cif, or by emailing data_request@ccdc.cam.ac.uk, or by contacting The Cambridge Crystallographic Data Centre, 12 Union Road, Cambridge CB2 1EZ, UK; fax: +44 1223 336033.

AUTHOR INFORMATION

Corresponding Authors

Andrew Ozarowski – National High Magnetic Field Laboratory, Tallahassee, Florida 32310, United States; orcid.org/0000-0001-6225-9796; Email: ozarowsk@magnet.fsu.edu

Kirill Kovnir – Department of Chemistry, Iowa State University, Ames, Iowa 50011, United States; Ames Laboratory, U.S. Department of Energy, Ames, Iowa 50011, United States; orcid.org/0000-0003-1152-1912; Email: kovnir@iastate.edu

Authors

Eranga H. Gamage – Department of Chemistry, Iowa State University, Ames, Iowa 50011, United States; Ames Laboratory, U.S. Department of Energy, Ames, Iowa 50011, United States; orcid.org/0000-0002-6954-7130

Raquel A. Ribeiro – Ames Laboratory, U.S. Department of Energy, Ames, Iowa 50011, United States; Department of Physics and Astronomy, Iowa State University, Ames, Iowa 50011, United States; orcid.org/0000-0001-6075-1701

Colin P. Harmer – Department of Chemistry, Iowa State University, Ames, Iowa 50011, United States; Ames Laboratory, U.S. Department of Energy, Ames, Iowa 50011, United States; orcid.org/0000-0003-0902-8731

Paul C. Canfield – Ames Laboratory, U.S. Department of Energy, Ames, Iowa 50011, United States; Department of Physics and Astronomy, Iowa State University, Ames, Iowa 50011, United States

Complete contact information is available at:

<https://pubs.acs.org/10.1021/acs.inorgchem.2c00298>

Funding

This research was supported by the National Science Foundation DMR-2003783 grant to K.K. This research used the resources at the beamline 17-BM and the mail-in program at the beamline 11-BM-B at the Advanced Photon Source, Argonne National Laboratory, supported by the U.S. Department of Energy, Office of Science, Office of Basic Energy Sciences, under Contract No. DE-AC02-06CH11357. Magnetic characterizations performed by R.A.R. and P.C.C. were supported by the Ames Laboratory, the US Department of Energy, Office of Science, Basic Energy Sciences, Materials Science and Engineering Division under contract No. DE-AC02-07CH11358. An EPR portion of this work was performed at the National High Magnetic Field Laboratory, which is supported by the National Science Foundation Cooperative Agreement No. DMR-1644779 and the State of Florida.

Notes

The authors declare no competing financial interest.

ACKNOWLEDGMENTS

The authors are thankful to the beamline scientists Dr. Andrey Yakovenko, Dr. Wenqian Xu, (17-BM), and Dr. Saul Lapidus (11-BM) at the APS ANL for their support in conducting the synchrotron experiments. They would also like to thank Dr. Warren Straszheim and Dr. Shannon Lee for their help with SEM/EDS data collection as well as Dr. Dinesh Amarasinghe for helping with the Rietveld refinement.

REFERENCES

- (1) Bleaney, B.; Bowers, K. D. Anomalous Paramagnetism of Copper Acetate. *Proc. R. Soc. Lond. A* **1952**, *214*, 451–465.
- (2) Ozarowski, A. The Zero-Field-Splitting Parameter D in Binuclear Copper(II) Carboxylates Is Negative. *Inorg. Chem.* **2008**, *47*, 9760–9762.
- (3) Maurice, R.; Sivalingam, K.; Ganyushin, D.; Guihéry, N.; Graaf, C. de.; Neese, F. Theoretical Determination of the Zero-Field Splitting in Copper Acetate Monohydrate. *Inorg. Chem.* **2011**, *50*, 6229–6236.
- (4) Reger, D. L.; Pascui, A. E.; Foley, E. A.; Smith, M. D.; Jezierska, J.; Wojciechowska, A.; Stoian, S. A.; Ozarowski, A. Dinuclear Metallacycles with Single M-X-M Bridges ($X = \text{Cl}^-$, Br^- ; $M = \text{Fe(II)}$, Co(II) , Ni(II) , Cu(II) , Zn(II) , Cd(II)): Strong Antiferromagnetic Superexchange Interactions. *Inorg. Chem.* **2017**, *56*, 2884–2901.
- (5) Klingele, J.; Dechert, S.; Meyer, F. Polynuclear Transition Metal Complexes of Metal...Metal-Bridging Compartmental Pyrazolate Ligands. *Coord. Chem. Rev.* **2009**, *253*, 2698–2741.
- (6) Casey, C. P.; Audett, J. D. Synthesis and Reactivity of Saturated Hydrocarbon-Bridged Dinuclear Complexes. *Chem. Rev.* **1986**, *86*, 339–352.
- (7) Holton, J.; Lappert, M. F.; Pearce, R.; W Yarrow, P. I. Bridged Hydrocarbyl or Hydrocarbon Binuclear Transition-Metal Complexes: Classification, Structures, and Chemistry. *Chem. Rev.* **1983**, *83*, 135–201.
- (8) Premužić, D.; Holyńska, M.; Ozarowski, A.; Pietzonka, C.; Roseborough, A.; A Stoian, S. Model Dimeric Manganese(IV) Complexes Featuring Terminal Tris-Hydroxotetraazaadamantane and Various Bridging Ligands. *Inorg. Chem.* **2020**, *59*, 10768–10784.
- (9) Delfs, C. D.; Stranger, R. Oxidation State Dependence of the Geometry, Electronic Structure, and Magnetic Coupling in Mixed Oxo- and Carboxylato-Bridged Manganese Dimers. *Inorg. Chem.* **2001**, *40*, 3061–3076.
- (10) Summerville, R. H.; Hoffmann, R. Tetrahedral and Other M_2L_6 Transition Metal Dimers. *J. Am. Chem. Soc.* **1976**, *98*, 7240–7254.
- (11) Weihe, H.; Gudel, H. U. Magneto-Structural Correlations in Linear and Bent Oxo-Bridged Transition-Metal Dimers: Comparisons, Interpretations, and Predictions of Ground-State Magnetic Properties. *J. Am. Chem. Soc.* **1998**, *120*, 2870–2879.
- (12) Lai, Y. K.; Wong, K. Y. Electrochemistry of Oxo-Bridged Ruthenium Dimers with 4,4'-Dichloro- and 5,5'-Dichloro-2,2'-Bipyridine and Their Catalytic Properties towards Water Oxidation. *J. Electroanal. Chem.* **1995**, *380*, 193–200.
- (13) Concepcion, J. J.; Jurss, J. W.; Templeton, J. L.; Meyer, T. J. Mediator-Assisted Water Oxidation by the Ruthenium "Blue Dimer" $cis,cis-[(bpy)_2(H_2O)RuORu(OH_2)(bpy)_2]^{4+}$. *Proc. Natl. Acad. Sci.* **2008**, *105*, 17632–17635.
- (14) Notaro, A.; Gasser, G. Monomeric and Dimeric Coordinatively Saturated and Substitutionally Inert Ru(II) Polypyridyl Complexes as Anticancer Drug Candidates. *Chem. Soc. Rev.* **2017**, *46*, 7317–7337.
- (15) Hess, J.; Keiser, J.; Gasser, G. Toward Organometallic Antischistosomal Drug Candidates. *Future Med. Chem.* **2015**, *7*, 821–830.
- (16) Padhi, S. K.; Rai, S.; Akhter, S. S. Redox-Induced Structural Switching through Sporadic Pyridine-Bridged $\text{Co}^{\text{II}}\text{Co}^{\text{II}}$ Dimer and Electrocatalytic Proton Reduction. *Inorg. Chem.* **2020**, *59*, 7810–7821.
- (17) Buvaylo, E. A.; Kokozay, V. N.; Vassilyeva, O. Y.; Skelton, B. W.; Ozarowski, A.; Titiš, J.; Vranovićová, B.; Boča, R. Field-Assisted Slow Magnetic Relaxation in a Six-Coordinate Co(II)-Co(III) Complex with Large Negative Anisotropy. *Inorg. Chem.* **2017**, *56*, 6999–7009.
- (18) Chandrasekhar, V.; Dey, A.; Mota, A. J.; Colacio, E. Slow Magnetic Relaxation in Co(III)-Co(II) Mixed-Valence Dinuclear Complexes with a $\text{Co}^{\text{II}}\text{O}_5\text{X}$ ($X = \text{Cl}$, Br , NO_3) Distorted-Octahedral Coordination Sphere. *Inorg. Chem.* **2013**, *52*, 4554–4561.
- (19) Brazzolotto, D.; Cantú Reinhard, F. G.; Smith-Jones, J.; Retegan, M.; Amidani, L.; Faponle, A. S.; Ray, K.; Philouze, C.; de Visser, S. P.; Gennari, M.; Duboc, C. A High-Valent Non-Heme μ -Oxo Manganese(IV) Dimer Generated from a Thiolate-Bound Manganese(II) Complex and Dioxygen. *Angew. Chem. Int. Ed.* **2017**, *56*, 8211–8215.
- (20) Shova, S.; Vlad, A.; Cazacu, M.; Krzystek, J.; Ozarowski, A.; Malček, M.; Bucinsky, L.; Rapta, P.; Cano, J.; Telsler, J.; Arion, V. B. Dinuclear Manganese(III) Complexes with Bioinspired Coordination and Variable Linkers Showing Weak Exchange Effects: A Synthetic, Structural, Spectroscopic and Computation Study. *Dalt. Trans.* **2019**, *48*, 5909–5922.
- (21) Liu, J.; Krzystek, J.; Hill, S.; Barrios, L.; Aromí, G. Elucidating Magnetic Exchange and Anisotropy in Weakly Coupled Mn^{III} Dimers. *Inorg. Chem.* **2013**, *52*, 718–723.
- (22) Reger, D. L.; Debreczeni, A.; Smith, M. D.; Jezierska, J.; Ozarowski, A. Copper(II) Carboxylate Dimers Prepared from Ligands Designed to Form a Robust $\pi\cdots\pi$ Stacking Synthone: Supramolecular Structures and Molecular Properties. *Inorg. Chem.* **2012**, *51*, 1068–1083.
- (23) Reger, D. L.; Pascui, A. E.; Smith, M. D.; Jezierska, J.; Ozarowski, A. Halide and Hydroxide Linearly Bridged Bimetallic Copper(II) Complexes: Trends in Strong Antiferromagnetic Superexchange Interactions. *Inorg. Chem.* **2012**, *51*, 7966–7968.
- (24) Triki, S.; Gómez-García, C. J.; Ruiz, E.; Sala-Pala, J. Asymmetric Azido-Copper(II) Bridges: Ferro- or Antiferromagnetic? Experimental and Theoretical Magneto-Structural Studies. *Inorg. Chem.* **2005**, *44*, 5501–5508.
- (25) Reger, D. L.; Pascui, A. E.; Smith, M. D.; Jezierska, J.; Ozarowski, A. Syntheses, Structural, Magnetic, and Electron Paramagnetic Resonance Studies of Monobridged Cyanide and Azide Dinuclear Copper(II) Complexes: Antiferromagnetic Superexchange Interactions. *Inorg. Chem.* **2015**, *54*, 1487–1500.
- (26) Nesterova, O. V.; Nesterov, D. S.; Jezierska, J.; Pombeiro, A. J. L.; Ozarowski, A. Copper(II) Complexes with Bulky N-Substituted Diethanolamines: High-Field Electron Paramagnetic Resonance, Magnetic, and Catalytic Studies in Oxidative Cyclohexane Amidation. *Inorg. Chem.* **2018**, *57*, 12384–12397.
- (27) Capdevila, M.; Clegg, W.; González-Duarte, P.; Jarid, A.; Lledós, A. Hinge Distortion in Platinum(II) Dimers with a Pt_2S_2 Ring. An Ab Initio Molecular Orbital Study. *Inorg. Chem.* **1996**, *35*, 490–497.
- (28) Gamelin, D. R.; Bominaar, E. L.; Kirk, M. L.; Wieghardt, K.; Solomon, E. I. Excited-State Contributions to Ground-State Properties of Mixed-Valence Dimers: Spectral and Electronic-Structural Studies of $[\text{Fe}_2(\text{OH})_3(\text{Tmtacn})_2]^{2+}$ Related to the $[\text{Fe}_2\text{S}_2]^+$ Active Sites of Plant-Type Ferredoxins. *J. Am. Chem. Soc.* **1996**, *118*, 8085–8097.
- (29) Crouse, B. R.; Meyer, J.; Johnson, M. K. Spectroscopic Evidence for a Reduced Fe_2S_2 Cluster with a $S = 9/2$ Ground State in Mutant Forms of Clostridium Pasteurianum 2Fe Ferredoxin. *J. Am. Chem. Soc.* **1995**, *117*, 9612–9613.
- (30) Beardwood, P.; Gibson, J. F. $[\text{Fe}_2\text{S}_2(\text{OAr})_4]^{2-}$: Iron-Sulphur Dimers with Terminal Phenolate Ligands. *J. Chem. Soc., Chem. Commun.* **1985**, *36*, 102–104.
- (31) Shakurov, G. S.; Tarasov, V. F. High-Frequency Tunable EPR Spectroscopy of Cr^{3+} in Synthetic Forsterite. *Appl. Magn. Reson.* **2001**, *21*, 597–605.
- (32) Gaister, A. V.; Konovalov, A. A.; Shakurov, G. S.; Subbotin, K. A.; Tarasov, V. F.; Zharikov, E. V. High-Frequency Two-Dimensional EPR Spectroscopy of Cr^{3+} and Ho^{3+} Dimers in Synthetic Forsterite. *Proc. SPIE* **2004**, *5478*, 46–54.

- (33) Bershov, L. V.; Gaite, J.-M.; Hafner, S. S.; Rager, H. Electron Paramagnetic Resonance and ENDOR Studies of Cr^{3+} - Al^{3+} Pairs in Forsterite. *Phys. Chem. Miner.* **1983**, *9*, 95–101.
- (34) Fraser, H. W. L.; Nichol, G. S.; Velmurugan, G.; Rajaraman, G.; Brechin, E. K. Magneto-Structural Correlations in a Family of Di-Alkoxo Bridged Chromium Dimers. *Dalt. Trans.* **2017**, *46*, 7159–7168.
- (35) Scaringe, R. P.; Hodgson, D. J.; Hatfield, W. E. Exchange Coupling in Di- μ -Hydroxo-Bridged Chromium(III) Dimers. *Transit. Met. Chem.* **1981**, *6*, 340–344.
- (36) Kremer, S. EPR Spectroscopic Study of $S = 1$, 2, and 3 Spin States of Tris(μ -Hydroxo)-Bridged Chromium(III) Dimers. *Inorg. Chem.* **1985**, *24*, 887–890.
- (37) Zhong-Hai, N.; Zhao, Y.-H.; Zheng, L.; Kou, H.-Z.; Cui, A.-L. A New Hydroxo-Bridged Chromium (III) Dimer $[\text{Cr}(\text{Saltn})\text{OH}]_2 \cdot 4\text{H}_2\text{O}$: Synthesis, Crystal Structure and Magnetic Properties. *Chin. J. Chem.* **2005**, *23*, 786–790.
- (38) Heinrichs, M. A.; Hodgson, D. J.; Michelsen, K.; Pedersen, E. Synthesis and Characterization of the Chromium(III) Dimer Bis(μ -hydroxo)bis[[N,N' -bis(2-pyridylmethyl)-1,2-ethanediamine]-chromium(III)] Perchlorate, [(bispicen)Cr(OH)]₂(ClO₄)₄·H₂O. *Inorg. Chem.* **1984**, *23*, 3174–3180.
- (39) Scaringe, R. P.; Hatfield, W. E.; Hodgson, D. J. Magnetic and Structural Characterization of the Chromium(III) Dimer Sodium Di- μ -hydroxobis[bis(oxalato)chromate(III)] Hexahydrate, Na₄[Cr(C₂O₄)₂OH]₂·6H₂O. *Inorg. Chim. Acta* **1977**, *22*, 175–183.
- (40) Morsing, T. J.; Weihe, H.; Bendix, J. Probing Effective Hamiltonian Operators by Single-Crystal EPR: A Case Study Using Dinuclear Cr(III) Complexes. *Inorg. Chem.* **2016**, *55*, 1453–1460.
- (41) McNeely, J.; Cage, B. DFT-BS Examination of Exchange Coupling in Chromium(III) Dimers Containing the $\mu_{1,2}$ -Squarato Bridge. *Inorg. Chim. Acta* **2012**, *384*, 189–196.
- (42) Tchougréeff, A. L.; Dronskowski, R. Effective Hamiltonian Crystal Field as Applied to Magnetic Exchange Parameters in μ -Oxo-Bridged Cr(III) Dimers. *J. Phys. Chem. A* **2013**, *117*, 7980–7988.
- (43) Morsing, T. J.; Sauer, S. P. A.; Weihe, H.; Bendix, J.; Døssing, A. Magnetic Interactions in Oxide-Bridged Dichromium(III) Complexes. Computational Determination of the Importance of Non-Bridging Ligands. *Inorg. Chim. Acta* **2013**, *396*, 72–77.
- (44) Charlot, M. F.; Kahn, O.; Drillon, M. Correlation Structure-Magnetic Properties in (Cr₂O₁₀)¹⁴⁻ Dimeric Units: A Theoretical Approach. *Chem. Phys.* **1982**, *70*, 177–187.
- (45) Semenaka, V. V.; Nesterova, O. V.; Kokozay, V. N.; Dyakonenko, V. V.; Zubatyuk, R. L.; Shishkin, O. V.; Boča, R.; Jezierska, J.; Ozarowski, A. Cr^{III}-Cr^{III} Interactions in Two Alkoxo-Bridged Heterometallic Zn₂Cr₂ Complexes Self-Assembled from Zinc Oxide, Reineckes Salt, and Diethanolamine. *Inorg. Chem.* **2010**, *49*, 5460–5471.
- (46) Chakraborty, U.; Urban, F.; Mü, B.; Rebreyend, C.; De Bruin, B.; Van Velzen, N.; Harder, S.; Wolf, R. Accessing the Cp^{Ar}Ni(I) Synthons: Reactions with N-Heterocyclic Carbenes, TEMPO, Sulfur, and Selenium. *Organometallics* **2016**, *35*, 1624–1631.
- (47) Nomura, M. Organometallic Dithiolene Complexes of the Group 8–10 Metals: Reactivities, Structures and Electrochemical Behavior. *Dalt. Trans.* **2011**, *40*, 2112.
- (48) Panda, C.; Menezes, P. W.; Walter, C.; Yao, S.; Miehlisch, M. E.; Gutkin, V.; Meyer, K.; Driess, M. From a Molecular 2Fe-2Se Precursor to a Highly Efficient Iron Diselenide Electrocatalyst for Overall Water Splitting. *Angew. Chem., Int. Ed.* **2017**, *56*, 10506–10510.
- (49) AzizpoorFard, M.; Levchenko, T. I.; Cadogan, C.; Humenny, W. J.; Corrigan, J. F. Stable -ESiMe₃ Complexes of CuI and AgI (E = S, Se) with NHCs: Synthons in Ternary Nanocluster Assembly. *Chem.-Eur. J.* **2016**, *22*, 4543–4550.
- (50) Marsden, C. J.; Sheldrick, G. M. The Crystal and Molecular Structure of Bis{ μ [(tri-fluoromethyl)seleno]manganese tetracarbonyl}. *J. Organomet. Chem.* **1972**, *40*, 183–186.
- (51) Song, L. C.; Cheng, H. W.; Hu, Q. M. Synthesis, Spectroscopic Characterization and Reactivities of Linear and Butterfly Chromium/Selenium Complexes Containing Substituted Cyclopentadienyl Ligands: Crystal Structures of [η^5 -MeC₅M₃H₄Cr(CO)₂]₂Se and [η^5 -EtO₂CC₃H₄Cr(CO)₂]₂Se₂. *J. Organomet. Chem.* **2004**, *689*, 1849–1855.
- (52) Wei, C.; Goh, L. Y.; Sinn, E. Chemistry of [CpCr(CO)₃]₂. An Insertion Mechanism for the Formation of Cp₂Cr₂(CO)₅Se₂ and Cp₂Cr₂(CO)₄Se₂ from Cp₂Cr₂(CO)₄Se. Carbonylation and Crystal Structure of Cp₂Cr₂(CO)₄Se₂. *Organometallics* **1988**, *7*, 2020–2026.
- (53) Goh, L. Y.; Wei, C.; Sinn, E. Mono- and Di-Selenium Complexes of Chromium. Syntheses and Crystal Structures of (η^5 -C₅H₅)₂Cr₂(CO)₄Se and (η^5 -C₅H₅)₂Cr₂(CO)₄Se₂. *J. Chem. Soc. Chem. Commun.* **1985**, 462–464.
- (54) Thiele, G.; Santner, S.; Donsbach, C.; Assmann, M.; Müller, M.; Dehnen, S. Solvothermal and Ionothermal Syntheses and Structures of Amine- and/or (poly-)Chalcogenide Coordinated Metal Complexes. *Z. Kristallogr. - Cryst. Mater.* **2014**, *229*, 489–495.
- (55) Gamage, E. H.; Greenfield, J. T.; Unger, C.; Kamali, S.; K Clark, J.; Harmer, C. P.; Luo, L.; Wang, J.; Shatruck, M.; Kovnir, K. Tuning Fe–Se Tetrahedral Frameworks by a Combination of [Fe(en)₃]²⁺ Cations and Cl⁻ Anions. *Inorg. Chem.* **2020**, *59*, 13353–13363.
- (56) Toby, B. H.; Von Dreele, R. B. GSAS-II: The Genesis of a Modern Open-Source All Purpose Crystallography Software Package. *J. Appl. Crystallogr.* **2013**, *46*, 544–549.
- (57) Sheldrick, G. M. Crystal Structure Refinement with SHELXL. *Acta Cryst. C* **2015**, *71*, 3–8.
- (58) Hassan, A. K.; Pardi, L. A.; Krzystek, J.; Sienkiewicz, A.; Goy, P.; Rohrer, M.; Brunel, L. C. Ultrawide Band Multifrequency High-Field EMR Technique: A Methodology for Increasing Spectroscopic Information. *J. Magn. Reson.* **2000**, *142*, 300–312.
- (59) Benelli, C.; Gatteschi, D. *Introduction to Molecular Magnetism: From Transition Metals to Lanthanides*; Wiley-VCH: Weinheim, Germany, 2015.
- (60) Kallesøe, S.; Pedersen, E. Magnetic Properties of the Chromium(III) Dimer Delta(-)₅₄₆-Di- μ -hydroxo(S,S,S,S)-tetrakis(L-prolinato)dichromium(III) Tetrahydrate. *Acta Chem. Scand.* **1982**, *A36*, 859–860.
- (61) Inoue, T.; Sugiyama, K.; Takeuchi, T.; Nakahanada, M.; Kaizaki, S.; Date, M. High Field Magnetization of Cr-Dimer Complexes. *J. Phys. Soc. Japan* **1992**, *61*, 4566–4571.
- (62) Ciornea, V.; Mingalieva, L.; Costes, J. P.; Novitchi, G.; Filippova, I.; Galeev, R. T.; Shova, S.; Voronkova, V. K.; Gulea, A. Structural Determinations, Magnetic and EPR Studies of Complexes Involving the Cr(OH)₂Cr Unit. *Inorg. Chim. Acta* **2008**, *361*, 1947–1957.
- (63) Scaringe, R. P.; Singh, P.; Eckberg, R. P.; Hatfield, W. E.; Hodgson, D. J. Structural and Magnetic Characterization of Di- μ -hydroxo-bis[bis(1,10-phenanthroline(chromium(III))] Iodide Tetrahydrate. *Inorg. Chem.* **1975**, *14*, 1127–1133.
- (64) Fischer, H. R.; Glerup, J.; Hodgson, D. J.; Pedersen, E. Structural and Magnetic Characterization of the Alkoxo-Bridged Chromium(III) Dimer Bis(μ -methoxy)bis[bis(2,4-pentanedionato)-chromium(III)], [(acac)₂Cr(OCH₃)₂]₂. *Inorg. Chem.* **1982**, *21*, 3063–3066.
- (65) Henning, J. C. M.; Damen, J. P. M. Exchange Interactions within Nearest-Neighbor Cr³⁺ Pairs in Chromium-Doped Spinel ZnGa₂O₄. *Phys. Rev. B* **1971**, *3*, 3852–3854.
- (66) Kartsev, A.; Augustin, M.; Evans, R. F. L.; Novoselov, K. S.; Santos, E. J. G. Biquadratic Exchange Interactions in Two-Dimensional Magnets. *NPJ Comput. Mater.* **2020**, *6*, 150.
- (67) Rodríguez-Fortea, A.; Alemany, P.; Alvarez, S.; Ruiz, E. Exchange Coupling in Halo-Bridged Dinuclear Cu(II) Compounds: A Density Functional Study. *Inorg. Chem.* **2002**, *41*, 3769–3778.
- (68) Onofrio, N.; Mouesca, J.-M. Analysis of the Singlet–Triplet Splitting Computed by the Density Functional Theory–Broken-Symmetry Method: Is It an Exchange Coupling Constant? *Inorg. Chem.* **2011**, *50*, 5577–5586.
- (69) Malrieu, J. P.; Caballol, R.; J Calzado, C.; de Graaf, C.; Guihéry, N. Magnetic Interactions in Molecules and Highly Correlated

Materials: Physical Content, Analytical Derivation, and Rigorous Extraction of Magnetic Hamiltonians. *Chem. Rev.* **2014**, *114*, 429–492.

(70) Noodleman, L.; Case, D. A. Density-Functional Theory of Spin Polarization and Spin Coupling in Iron–Sulfur Clusters. In *Advances in Inorganic Chemistry*, 1992; Vol. 38, pp. 423–458.

(71) Noodleman, L.; Davidson, E. R. Ligand Spin Polarization and Antiferromagnetic Coupling in Transition Metal Dimers. *Chem. Phys.* **1986**, *109*, 131–143.

(72) Noodleman, L. Valence Bond Description of Antiferromagnetic Coupling in Transition Metal Dimers. *J. Chem. Phys.* **1981**, *74*, 5737–5743.

(73) Neese, F. The ORCA Program System. *Wiley Interdiscip. Rev. Comput. Mol. Sci.* **2012**, *2*, 73–78.

(74) Roos, B. O.; Taylor, P. R.; Sigbahn, P. E. M. A Complete Active Space SCF Method (CASSCF) Using a Density Matrix Formulated Super-CI Approach. *Chem. Phys.* **1980**, *48*, 157–173.

(75) Angeli, C.; Cimiraglia, R.; Evangelisti, S.; Leininger, T.; Malrieu, J.-P. Introduction of N-Electron Valence States for Multireference Perturbation Theory. *J. Chem. Phys.* **2001**, *114*, 10252.

(76) Neese, F. Calculation of the Zero-Field Splitting Tensor on the Basis of Hybrid Density Functional and Hartree-Fock Theory. *J. Chem. Phys.* **2007**, *127*, 164112.

Recommended by ACS

Meeting the Challenge of Magnetic Coupling in a Triply-Bridged Chromium Dimer: Complementary Broken-Symmetry Density Functional Theory and M...

Dimitrios A. Pantazis.

JANUARY 15, 2019
JOURNAL OF CHEMICAL THEORY AND COMPUTATION

READ 

Degradation Chemistry and Kinetic Stabilization of Magnetic CrI3

Taiming Zhang, Jiong Lu, *et al.*

MARCH 16, 2022
JOURNAL OF THE AMERICAN CHEMICAL SOCIETY

READ 

Breaking the Magic Border of One Second for Slow Magnetic Relaxation of Cobalt-Based Single Ion Magnets

Roman Boča, Dušan Valigura, *et al.*

NOVEMBER 08, 2018
INORGANIC CHEMISTRY

READ 

Discovery of a Dysprosium Metallocene Single-Molecule Magnet with Two High-Temperature Orbach Processes

Fu-Sheng Guo, Richard A. Layfield, *et al.*

APRIL 14, 2022
INORGANIC CHEMISTRY

READ 

Get More Suggestions >